



GR focus review

Tectonic framework of the northern Junggar Basin Part II: The island arc basin system of the western Luliang Uplift and its link with the West Junggar terrane

Di Li ^a, Dengfa He ^{a,*}, M. Santosh ^b, Delong Ma ^a^a *The Key Laboratory of Marine Reservoir Evolution and Hydrocarbon Accumulation Mechanism, the Ministry of Education, China University of Geosciences, Beijing 100083, China*^b *School of Earth Sciences and Resources, China University of Geosciences, Beijing 100083, China*

ARTICLE INFO

Article history:

Received 16 April 2014

Received in revised form 19 July 2014

Accepted 18 August 2014

Available online 2 October 2014

Handling Editor: W.J. Xiao

Keywords:

Island arc basin system

Geochemical and geophysical data

Western Luliang Uplift

West Junggar terrane

Central Asian Orogenic Belt

ABSTRACT

Late Paleozoic tectonic links between Luliang Uplift and the adjacent West Junggar terrane remain poorly understood, despite their significant implications for the tectonic reconstruction of Junggar terrane and its role in the evolution of the Central Asian Orogenic Belt. The western Luliang Uplift offers a critical window to address this problem. In this study, based on seismic profiles and geophysical interpretation of the western Luliang Uplift, and from new geochronological and geochemical data, we evaluate the tectonostratigraphic evolution of the region. The western Luliang Uplift is composed of Carboniferous basalt, andesite and dacite interbedded with multiple layers of siltstone and mudstone. Zircon U–Pb isotopic data indicate that these rocks coevally erupted in 323–327 Ma. Seismic profile across the tectonic belt shows that the western Luliang Uplift experienced a structural inversion from Carboniferous extension to latest Carboniferous–Early Permian compression. The basalts and andesites show tholeiitic to calc-alkaline affinity, high $\epsilon_{\text{Nd}}(t)$ (6.4–8.0) and low initial $^{87}\text{Sr}/^{86}\text{Sr}$ (0.703497–0.704826), relative enrichment in LILEs and REEs, and depletion in HFSEs, especially Nb, Ta and Ti. The dacites show arc-like geochemical characteristics comparable with I-type granite, and positive $\epsilon_{\text{Nd}}(t)$ (4.8–4.9) and $\epsilon_{\text{Hf}}(t)$ (4.1–9.9) values. These features indicate that the basaltic rocks and dacites were derived from partial melting of a depleted mantle modified by slab-derived fluids and a juvenile lower crust respectively in an island arc environment during the Early Carboniferous. Furthermore, these coeval volcanic rocks show a temporal variation of tholeiitic to calc-alkaline series in the south to calc-alkaline to shoshonitic series in the north, together with extensional deformation and formation of the volcano-sedimentary sequence. These features suggest that the western Luliang Uplift was dominated by northward subduction with forearc and intra-arc basin in the Early Carboniferous. The Middle Permian terrigenous strata unconformably overlie the Early Carboniferous strata, indicating that the ocean basin might have closed during the Early Permian. Similarities in the tectonostratigraphic evolution show that the western Luliang Uplift and southern West Junggar terrane share a common tectonic evolution from Carboniferous subduction–accretion process to Early Permian amalgamation, further confirming the Luliang Uplift as an important link between the East and West Junggar terranes.

© 2014 International Association for Gondwana Research. Published by Elsevier B.V. All rights reserved.

Contents

1. Introduction	1111
2. Geological background	1113
3. Structural deformation and stratigraphic successions of the western Luliang Uplift	1114
4. Analytical methods	1117
4.1. Zircon SIMS U–Pb dating	1117
4.2. Major and trace element analyses	1117
4.3. The whole rock Sr–Nd analyses	1117
4.4. In-situ Lu–Hf isotopic analyses	1118
5. Analytical results	1118
5.1. Zircon U–Pb dating results	1118
5.2. Major oxides and trace elements	1119

* Corresponding author. Tel.: +86 10 82323868; fax: +86 10 82326850.

E-mail addresses: xdldi@163.com (D. Li), hedengfa282@263.net (D. He).

5.3. Whole rock Sr–Nd isotope compositions	1119
5.4. In-situ zircon Lu–Hf isotope compositions	1120
6. Discussion	1120
6.1. Early Carboniferous northward subduction-related basin system	1120
6.2. Tectonic link with the West Junggar terrane and its implication	1124
7. Conclusions	1126
Acknowledgments	1127
References	1127

1. Introduction

The successive accretion of oceanic islands, seamounts, accretionary wedges and microcontinents from Neoproterozoic to Late Paleozoic resulted in the formation of the Central Asian Orogenic Belt (CAOB) which extends from the Urals to the Pacific Ocean between the main continents of Baltica, Siberia, Tarim and North China (Şengör et al., 1993; Buslov et al., 2001; Jahn et al., 2004; Windley et al., 2007; Xiao et al., 2008; Safonova et al., 2009; Xiao et al., 2009, 2010; Rojas-Agramonte

et al., 2011; Safonova et al., 2011; Wilhem et al., 2012; Kröner et al., 2013; Xiao et al., 2013; Xiao and Santosh, 2014) (Fig. 1a). The CAOB represents the largest area of Phanerozoic crustal growth in the world and more than 50% of its growth is considered to have involved the addition of mantle-derived juvenile material (Jahn et al., 2000; Kovalenko et al., 2004; Kröner et al., 2014), driven by the long-lasting (ca. 800 Ma) evolution and closure of the Paleo-Asian Ocean (PAO) (Xiao et al., 2009; Wilhem et al., 2012). The voluminous Paleozoic strata deposited within sedimentary basin, and their structural deformation patterns carry

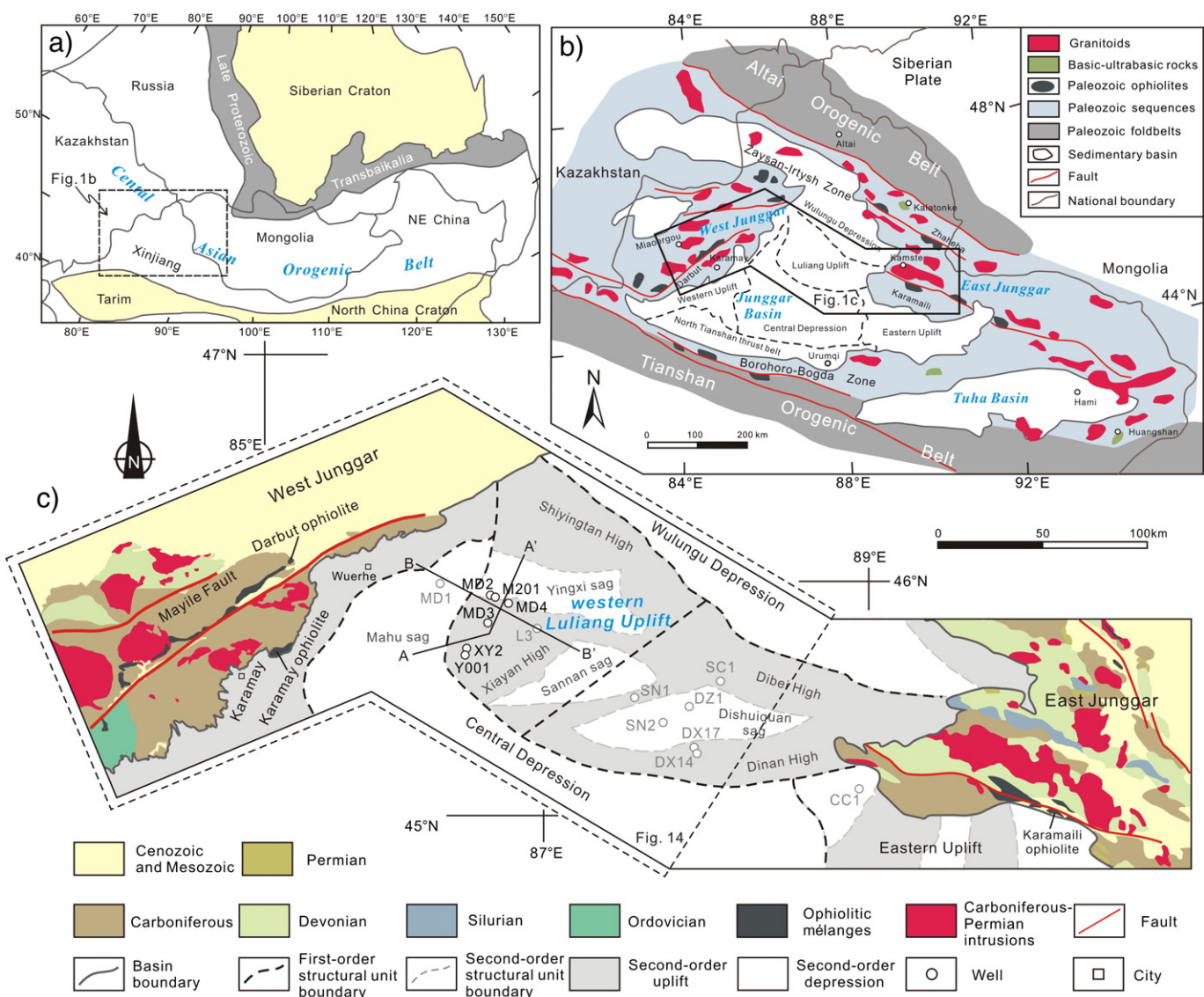


Fig. 1. (a) The relationship of the Junggar terrane with the Central Asian Orogenic Belt (modified from Jahn et al. (2004); and Windley et al. (2007)). (b) Simplified geological map of the Junggar terrane in northern Xinjiang (modified from Chen and Jahn (2004)). (c) Map of Luliang Uplift and adjacent East and West Junggar terranes showing the location of six boreholes and gravity and magnetic data used for this study. Two bold solid lines represent the location of seismic profiles (AA' and BB').

important information on the crustal growth and the complex tectonic history associated with one of the largest accretionary orogens of the world.

The Junggar Basin is located in the southern margin of the CAOB (Fig. 1b), at the loci of the East and West Junggar terranes, and has been a critical area to study the formation process and mechanisms of accretionary orogens and crustal growth (Yakubchuk, 2004; Seltmann and Porter, 2005; Windley et al., 2007; Kröner et al., 2008; Shen et al., 2010; Xiao et al., 2013; Xiao and Santosh, 2014). An increasing number of Hf–Nd isotopic data of Paleozoic rocks from the Junggar Basin have provided new evidence that attests to the absence of Precambrian continental rocks (Wang et al., 2002; Zheng et al., 2007; Su et al., 2010; He et al., 2013). Based on geological, geochronological, geochemical and geophysical data, some workers proposed that the basement of the Junggar Basin may be mostly composed of arcs, accretionary complexes and trapped oceanic crust in the Late Paleozoic (Carroll et al., 1990; Hu et al., 2000; Chen and Jahn, 2004; Zheng et al., 2007; Xiao et al., 2008), suggesting that the Junggar Basin experienced intra-oceanic subduction and accretion process during this period, which is consistent with the Late Devonian to Early Carboniferous island-arc setting in the East and West Junggar terranes (Shen et al., 2009; Geng et al., 2011; Xiao et al., 2011; Su et al., 2012; X.W. Xu et al., 2013). The bimodal volcanic rocks, A-type granites and molasses indicate that the ocean basin in the East and West Junggar terranes closed during the Late Carboniferous–Middle Permian (Han et al., 2006; Zhou et al., 2008; Chen et al.,

2010; Yang et al., 2011). Nevertheless, recent studies on the eastern Luliang Uplift suggest that the subduction-related setting in the Junggar Basin might have continued into the Late Carboniferous as a northward subduction, which is also supported by our geophysical and geochemical data (Li et al., 2014, 2015-b), suggesting that the closure time of PAO in the Junggar Basin is likely to be later than those represented by the present peripheral mountains. Although the basic tectonic framework in space and time during Carboniferous in the Junggar Basin has been well established (X.F. Yang et al., 2012; He et al., 2013), the previous studies were mainly concentrated on Carboniferous strata from the eastern Luliang Uplift (Wu et al., 2009; Su et al., 2010; X.F. Yang et al., 2012) and southern Junggar Basin (He et al., 2013), with only little attention focused on the western Luliang Uplift that connects the NW-trending Karamaili–Luliang tectonic zone and NE-trending Darbut tectonic zone and hence regarded as a key study area for paleotectonic reconstruction and continental growth mechanism of the Junggar terrane (Fig. 1c).

In this paper, we report the composition and distribution of Carboniferous stratigraphic sequence and associated deformational features of the western Luliang Uplift. We present results from whole rock Sr–Nd isotopic geochemistry and SIMS U–Pb ages and Lu–Hf isotopic compositions of zircon grains from the magmatic rocks from several boreholes in the basin. Our aims are to provide constraints on the Carboniferous tectonic evolution of the western Luliang Uplift and to discuss its link with the West Junggar terrane. Our data provide important constraints on

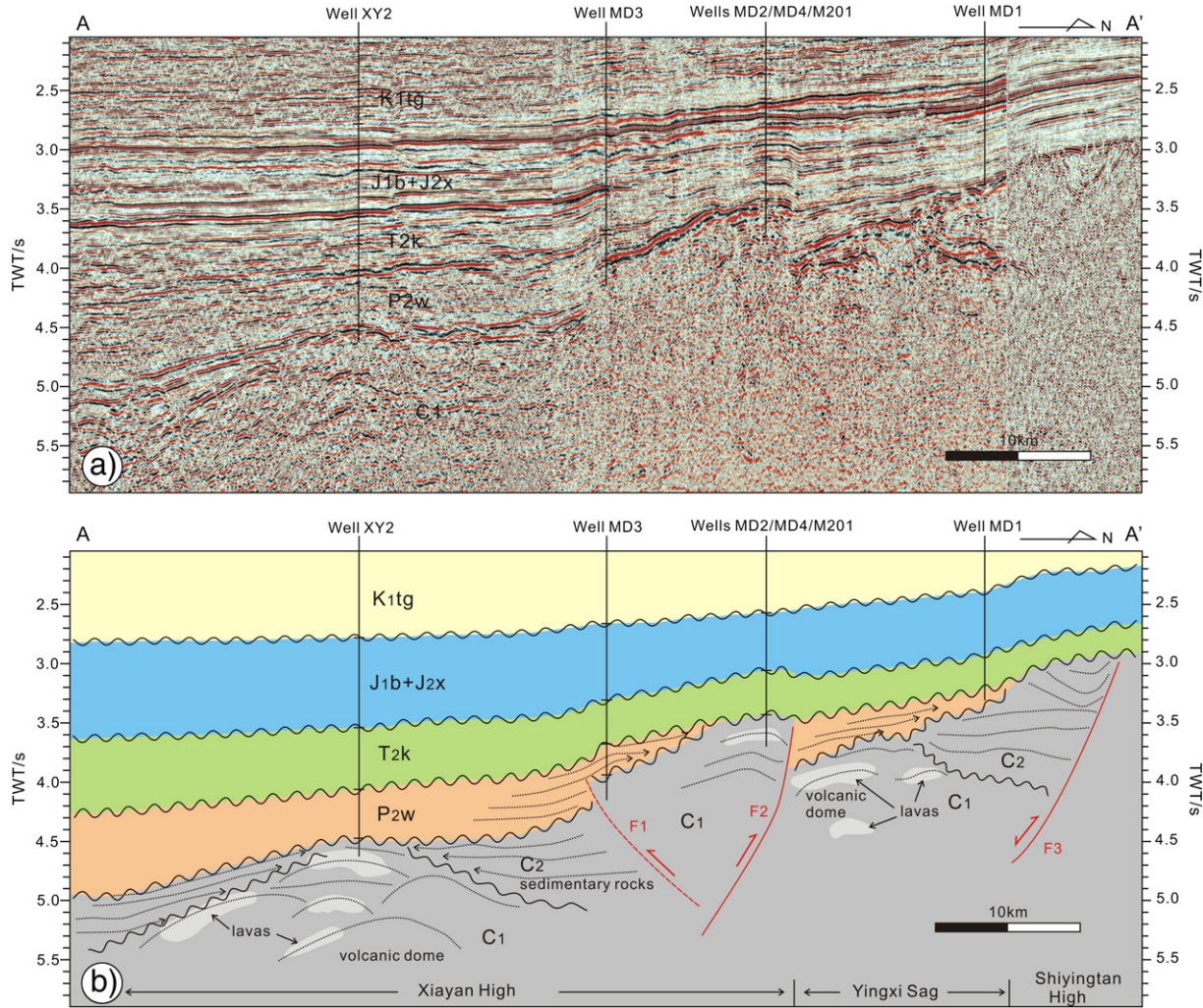


Fig. 2. Seismic profile AA' and its geological interpretation in the western Luliang Uplift. K₁tg—Lower Cretaceous Tugulu Group; J_{1b}—Lower Jurassic Badaowan Formation; J_{2x}—Middle Jurassic Xishanyao Formation; T_{2k}—Middle Triassic Karamay Formation; P_{2w}—Middle Permian Wuerhe Formation; C₂—Upper Carboniferous system; and C₁—Lower Carboniferous system.

the palinspastic restoration of the Junggar Basin, and have significant implications for understanding the continental growth of Central Asia.

2. Geological background

The Junggar terrane is located in the southern part of the CAOB and is bounded by the Kazakhstan and Siberian plates and the Tianshan Mountains. The Junggar terrane is traditionally divided into the East Junggar terrane, West Junggar terrane and Junggar Basin (Fig. 1b). The East Junggar terrane consists of Paleozoic arcs and accretionary complexes that were generated by subduction–accretion processes (Coleman, 1989; Xiao et al., 2009; Long et al., 2012; X.W. Xu et al., 2013). Two highly deformed and dismembered belts of ophiolite, the northern Zhaheba and the southern Karamaili ophiolite belts (Fig. 1b), are exposed in the East Junggar terrane along NW–SE trending faults. The zircon grains show SHRIMP U–Pb ages of 373 ± 10 to 336 ± 4 Ma for the Karamaili ophiolite (Jian et al., 2005; Tang et al., 2007) and 503 ± 10 to 481 ± 5 Ma for the Zhaheba ophiolite (Jian et al., 2003; Xiao et al., 2006). The West Junggar terrane is dominantly composed of Paleozoic accretionary complexes in the south and volcanic arcs in the north (Windley et al., 2007; Xiao et al., 2008; Zhang et al., 2011a, b). A marked feature of this region is the presence of Cambrian to Carboniferous ophiolitic mafic–ultramafic rocks with ages ranging from 577 ± 9 (G.X. Yang et al., 2012) to 332 ± 14 Ma (Xu et al., 2006), indicating a long-lived accretionary history since Cambrian. Carboniferous volcanic–sedimentary strata, including those of the Talegula, Baogutu and Xibeikulasi Formations, are widespread at both sides of the Darbut

ophiolite and are distributed in the southern East Junggar terrane along NE-trending faults. These rocks are dated as 391 ± 6 Ma using LA-ICP-MS U–Pb zircon method by G.X. Yang et al. (2012). The Paleozoic strata with voluminous volcanic rocks in the East and West Junggar terrane are widely invaded by Late Carboniferous to Permian granitoid and mafic intrusions (Chen and Jahn, 2004; Han et al., 2006; Chen et al., 2010; Q.Q. Xu et al., 2013).

The Junggar Basin, located between the East and West Junggar terranes, covers an area of $\sim 137,000$ km 2 and is filled by thick Paleozoic volcanic–sedimentary sequences and Mesozoic–Cenozoic sedimentary rocks. The Junggar Basin shows similar characteristics of magnetic and gravity gradients with those in the East and West Junggar terrane, suggesting a common geological structure (Li et al., 2014). Based on the structural features of the Upper Paleozoic units, the triangle-shaped Junggar basin is subdivided into four main first-order tectonic units from north to south, namely the Wulungu Depression, the Luliang Uplift, the Central Depression and the north Tianshan thrust belt (Bian et al., 2010) (Fig. 1b). The fossil records and isotopic ages show that Carboniferous and Permian strata occur widely in the basin, particularly in the Luliang Uplift (Wang et al., 2002; Zheng et al., 2007; X.F. Yang et al., 2012). The Carboniferous strata involve three units: the lower volcanic unit followed by sedimentary unit and the upper volcanic unit. The lower volcanic unit is dominated by andesite, dacite, rhyolite and tuff intercalated with minor basalt, whereas the upper volcanic unit is composed of basalt, andesite, rhyolite, tuff with minor clastic sedimentary rocks. Zircon grains from the tuff in the lower volcanic unit are dated at 337.2 Ma using SHRIMP U–Pb method, and the middle

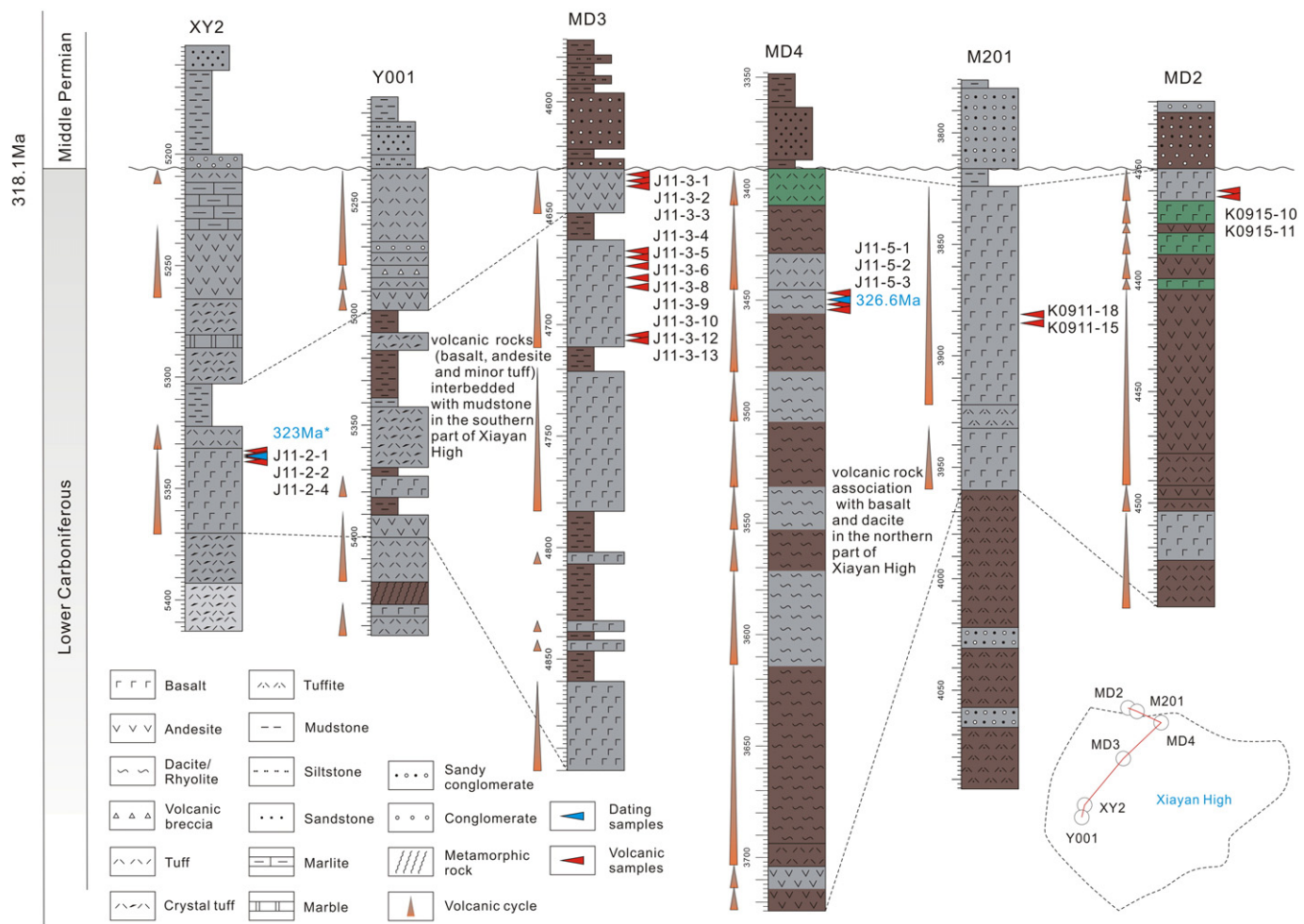


Fig. 3. The temporal and spatial distribution of Carboniferous strata in the western Luliang Uplift. Zircon Rb–Sr age (323 Ma) of basalt obtained from well XY2 is from Wang et al. (2002). Different colors represent the petrological colors as obviousness in Fig. 4a.

sedimentary and upper volcanic units belong to Upper Carboniferous. The Late Carboniferous tholeiitic basalts with high $\epsilon_{\text{Nd}}(t)$ values were considered to form in an extensional environment resulting from slow rollback of the subducting Junggar oceanic slab (Li et al., 2014, 2015-b). Although some authors consider that the East and West Junggar terranes had been in the post-collisional phase since ca. 340 Ma (Chen and Jahn, 2004; Han et al., 2006; Su et al., 2006; Zhou et al., 2008; Chen et al., 2010), the above information suggests that a subduction-related tectonic setting potentially existed in the Junggar Basin during Carboniferous.

3. Structural deformation and stratigraphic successions of the western Luliang Uplift

The western Luliang Uplift connects the NW-trending Karamaili-Luliang Uplift tectonic zone and the NE-trending West Junggar terrane.

The region is marked by a ~5 km thick Carboniferous–Cenozoic sedimentary sequence. The western Luliang Uplift is divided into three second-order tectonic units: the Xiayan High, Yingxi Sag and Shiyingtan High from south to north (Fig. 1c).

These tectonic units show NW-trending distribution, and might extend to the eastern Luliang Uplift. The Yingxi Sag, Sannan Sag and Dishuiquan Sag represent the same sag during Paleozoic. The NEE or EW-trending salients in the Luliang Uplift that divided the former sag resulted from Jurassic northwest oriented shortening (X.F. Yang et al., 2012). Seismic imaging provides useful information on the subsurface architecture of sedimentary basins and has been widely employed (Bally, 1983; Weimer and Davis, 1996). High-resolution seismic reflection along the profile AA' across the western Luliang Uplift shows (Fig. 1c) that there is a significant unconformity located between the Carboniferous and Permian (Fig. 2). The Carboniferous–Permian strata

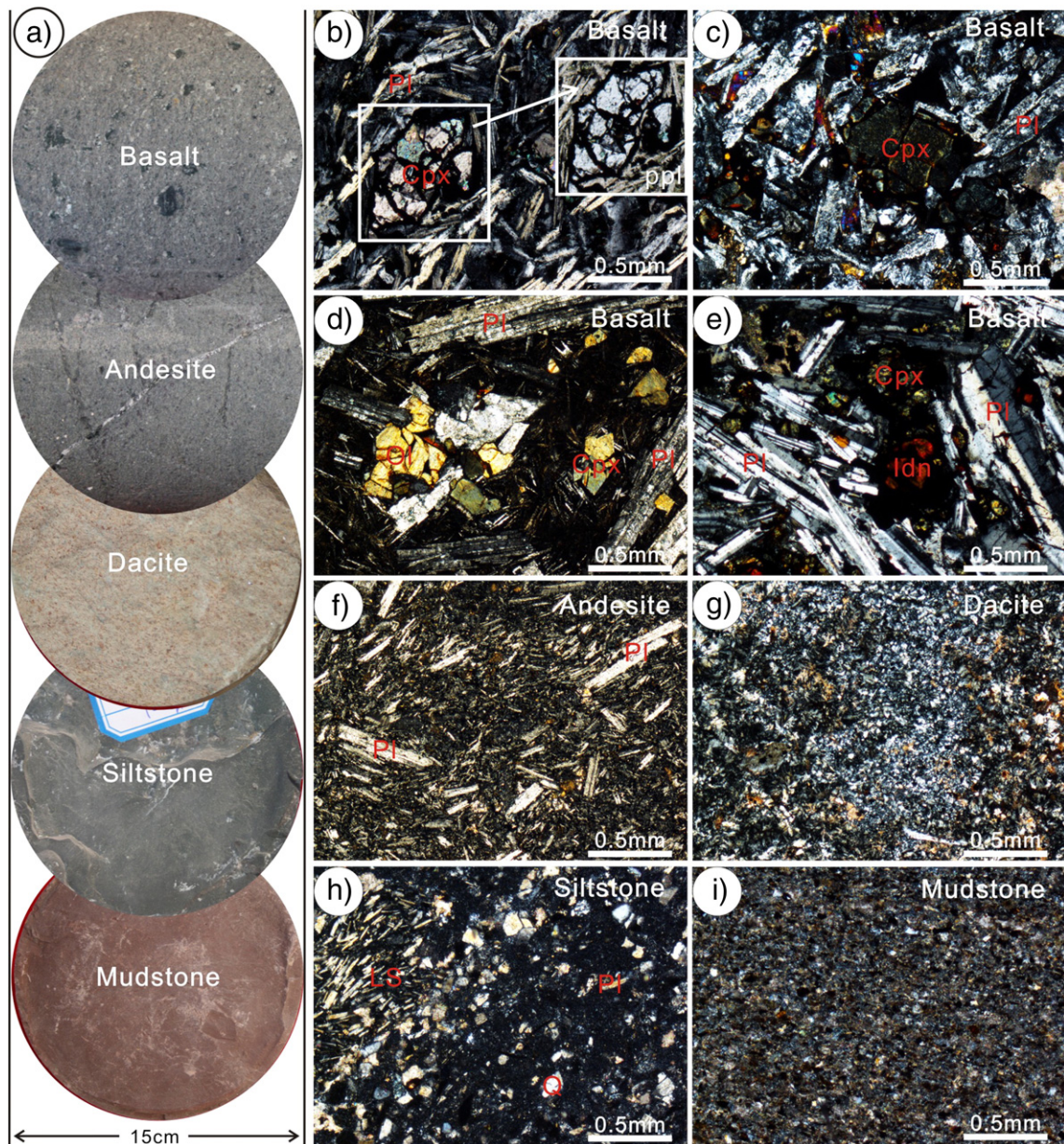


Fig. 4. Xiayan High petrological characteristics and photomicrographs (crossed nicols) of the Carboniferous borehole samples in the western Luliang Uplift. (a) Carboniferous rock association of western Luliang Uplift. (b) Intergranular texture with pyroxene and plagioclase in basalt from well XY2; (c) porphyritic texture with clinopyroxene and plagioclase phenocrysts in basalt from well MD3; (d) olivine-bearing basalt from well M201; (e) intergranular texture in iddingsite-bearing basalt from well MD2; (f) porphyritic texture with radial plagioclase phenocrysts and plagioclase microcrystal groundmass in andesite from well MD3; (g) felsitic texture with minor plagioclase phenocrysts in dacite from well MD4; (h) lithic fragment with abundant feldspar microcrystals in siltstone from well Y001; (i) mudstone from well Y001. PI – plagioclase; Cpx – clinopyroxene; Ol – olivine; Q – quartz; Idn – iddingsite; LS – lithic shreds; ppl – plane-polarized light.

in the Xiayan High are involved in NW trending and opposite-dipping high angle faults (e.g., F1, F2 and F3) (Fig. 2). Overall, the Carboniferous strata show thickening toward fault surface (F3), with the appearance of inverse structural deformation during the period of the latest Carboniferous to Early Permian, indicating a tectonic transition from extension to compression. The Middle Permian formation shows an evident overlap with the Carboniferous strata during the latest Carboniferous to Early Permian uplift and exhumation event. Strong thrusting during Permian (F1 and F2), and Mesozoic multiple unconformities probably resulted from the inversion or the rejuvenation of large-scale previous thrusts (Fig. 2).

All the wells in the Xiayan High mainly go through Middle Permian and part of Carboniferous except for Mesozoic–Cenozoic (Fig. 3). The Carboniferous strata are composed mainly of basalt, andesite, dacite, tuff, sandstone, mudstone and minor marlomite and marble. However, these rocks show heterogeneous distribution in the Xiayan High. The southern part is predominantly made up of basalt and andesite interbedded with mudstone/marlomite and minor metamorphic rocks, whereas the northern part comprises basalt, dacite and minor volcaniclastic rocks. In general, a period of volcanic activity shows the cycle of a volcano from eruption to lava gushes. According to the eruption-and-gushing-out model, the northern part of Xiayan High involves several periods of volcanic activity than its southern part, suggesting that frequent volcanic activity occurred in the northern part during the Carboniferous (Fig. 3). The Carboniferous basalts and andesites in the Xiayan High are gray colored and show weak chloritization (Fig. 4a). They display porphyritic texture dominated by phenocrysts of plagioclase and clinopyroxene and minor olivine, hornblende and iddingsite (Fig. 4b, c, d and e). Their groundmass is mainly composed of plagioclase with minor clinopyroxene and Fe–Ti oxides (Fig. 4c, e). The andesites consist of phenocrysts showing radial arrangement of plagioclase and microcrystals of plagioclase and augite in a fine-grained groundmass containing several magnetite grains (Fig. 4f), similar to the composition of typical basaltic andesites. The dacites are buff colored and show typical felsitic texture with minor plagioclase phenocrysts and a felsic and glassy groundmass (Fig. 4g). The sandstones are celadon in color and contain angular grains of medium sphericity that are mainly feldspar, quartz and volcanic lithic fragments with abundant feldspar microcrystals (Fig. 4h), and the microscopic debris of the mudstones are composed of muddy and feldspar grains, as well as small amounts of ash (Fig. 4i). The Middle Permian sandstone and mudstone unconformably overlie the Carboniferous strata (Fig. 3).

Table 1
SIMS U–Pb data of zircons for the dacite from the western Luliang Uplift.

Spots	U (ppm)	Th (ppm)	Th/U	^{206}Pb (ppm)	$^{207}\text{Pb}/^{206}\text{Pb}$ ±%	$^{207}\text{Pb}/^{235}\text{U}$ ±%	$^{238}\text{U}/^{206}\text{Pb}$ ±%	$^{207}\text{Pb}/^{206}\text{Pb}$ Age ± σ (Ma)	$^{207}\text{Pb}/^{235}\text{U}$ Age ± σ (Ma)	$^{206}\text{Pb}/^{238}\text{U}$ Age ± σ (Ma)
J11-5-1@1	174	104	0.6	11	0.0531 ± 2.2	0.3857 ± 2.7	0.0527 ± 1.5	333.0 ± 50	331.2 ± 7.6	331.0 ± 4.9
J11-5-1@2	88	53	0.6	6	0.0518 ± 3.1	0.3715 ± 3.4	0.0520 ± 1.5	275.7 ± 69	320.8 ± 9.4	327.5 ± 5.0
J11-5-1@3	210	190	0.9	14	0.0524 ± 2.9	0.3721 ± 3.2	0.0515 ± 1.5	304.6 ± 64	321.2 ± 8.9	325.9 ± 4.9
J11-5-1@4	412	318	0.8	27	0.0528 ± 1.5	0.3663 ± 2.1	0.0503 ± 1.5	321.4 ± 33	316.9 ± 5.7	316.3 ± 4.7
J11-5-1@5	553	942	1.7	47	0.0525 ± 1.4	0.3860 ± 2.1	0.0533 ± 1.5	308.7 ± 32	331.4 ± 5.9	337.3 ± 5.0
J11-5-1@6	441	538	1.2	34	0.0529 ± 1.4	0.3946 ± 2.0	0.0541 ± 1.5	322.8 ± 30	337.7 ± 5.8	340.0 ± 5.0
J11-5-1@7	204	112	0.6	13	0.0518 ± 2.2	0.3817 ± 2.7	0.0534 ± 1.5	277.9 ± 50	328.3 ± 7.5	336.0 ± 5.0
J11-5-1@8	262	176	0.7	17	0.0506 ± 3.0	0.3559 ± 3.4	0.0510 ± 1.5	221.7 ± 69	309.2 ± 9.1	321.8 ± 4.8
J11-5-1@9	395	419	1.1	29	0.0523 ± 1.7	0.3786 ± 2.3	0.0525 ± 1.5	297.1 ± 39	326.0 ± 6.4	330.4 ± 4.9
J11-5-1@10	249	181	0.7	16	0.0534 ± 1.8	0.3682 ± 2.4	0.0500 ± 1.5	345.5 ± 41	318.3 ± 6.5	314.4 ± 4.7
J11-5-1@11	137	79	0.6	9	0.0537 ± 2.4	0.3835 ± 2.8	0.0518 ± 1.5	357.2 ± 53	329.6 ± 8.0	325.4 ± 4.9
J11-5-1@12	211	138	0.7	14	0.0519 ± 2.0	0.3788 ± 2.5	0.0530 ± 1.5	278.7 ± 44	326.2 ± 6.9	333.4 ± 5.0
J11-5-1@13	254	195	0.8	16	0.0540 ± 1.8	0.3664 ± 2.4	0.0492 ± 1.5	371.8 ± 40	317.0 ± 6.4	309.0 ± 4.6
J11-5-1@14	241	201	0.8	17	0.0527 ± 2.1	0.3865 ± 2.6	0.0532 ± 1.5	315.3 ± 47	331.8 ± 7.4	336.6 ± 5.0
J11-5-1@15	134	112	0.8	9	0.0543 ± 2.4	0.3855 ± 2.9	0.0515 ± 1.5	383.6 ± 54	331.1 ± 8.1	323.1 ± 4.8
J11-5-1@16	196	89	0.5	12	0.0519 ± 2.3	0.3762 ± 2.8	0.0526 ± 1.5	280.0 ± 52	324.2 ± 7.7	330.9 ± 4.9
J11-5-1@17	281	182	0.7	18	0.0520 ± 1.7	0.3677 ± 2.3	0.0513 ± 1.5	283.9 ± 39	317.9 ± 6.2	322.9 ± 4.8
J11-5-1@18	257	248	1.0	18	0.0533 ± 1.8	0.3839 ± 2.3	0.0522 ± 1.5	342.7 ± 39	329.9 ± 6.6	328.0 ± 4.9
J11-5-1@19	165	125	0.8	11	0.0545 ± 3.0	0.3947 ± 3.4	0.0525 ± 1.5	391.0 ± 66	337.8 ± 9.8	331.8 ± 5.0
J11-5-1@20	329	240	0.7	22	0.0546 ± 1.5	0.3950 ± 2.2	0.0524 ± 1.5	397.7 ± 34	338.0 ± 6.2	328.7 ± 4.9

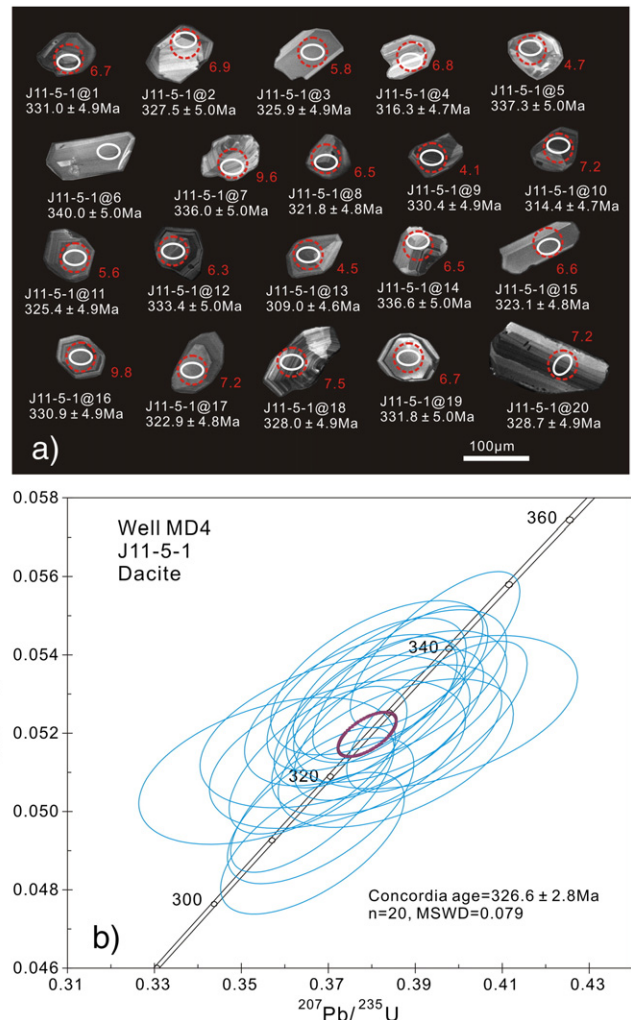


Fig. 5. Cathodoluminescence (CL) images of the analyzed zircon grains (a) and zircon SIMS U–Pb concordia diagram of dacite (J11-05-1) from well MD4 (b). The analytical spots for dated grains are shown as white circles, and the red circles represent in-situ Lu–Hf analysis spots.

Table 2

Major element (%) and trace elements (ppm) analyses of the Early Carboniferous volcanic rocks from the western Luliang Uplift.

Sample	J11-2-1	J11-2-2	J11-2-4	J11-3-1	J11-3-2	J11-3-3	J11-3-4	J11-3-5	J11-3-6	J11-3-8	J11-3-9	J11-3-10	J11-3-12	J11-3-13	K0911-15	K0911-18	K0915-10	K0915-11	J11-5-1	J11-5-2	J11-5-3
Well	XY2	XY2	XY2	MD3	MD3	MD3	MD3	MD3	MD3	MD3	MD3	MD3	MD3	MD3	M201	M201	MD2	MD2	MD4	MD4	MD4
Rock	basalt	basalt	basalt	basaltic andesite	basaltic andesite	basaltic andesite	basaltic andesite	basalt	basalt	basalt	basalt	basalt	basalt	basalt	basalt	basalt	basalt	basalt	rhyolite	rhyolite	rhyolite
Depth(m)	5332.1	5333.4	5335.8	4633.6	4636.0	4637.2	4638.1	4676.6	4677.5	4678.4	4679.4	4680.1	4701.8	4707.3	3885.6	3882.3	4360.9	4362.2	3449.5	3451.2	3454.9
SiO ₂	44.85	43.69	47.44	51.95	53.99	53.77	52.27	46.88	46.26	48.78	46.43	48.20	47.71	47.51	45.43	44.62	48.67	48.16	77.44	77.95	74.12
TiO ₂	1.85	1.95	1.91	2.49	2.13	2.38	2.56	1.81	1.98	2.03	2.20	1.91	1.97	1.88	1.92	2.18	2.12	2.15	0.20	0.21	0.27
Al ₂ O ₃	17.56	17.70	17.64	16.04	15.78	15.28	16.19	16.36	16.43	17.92	16.41	16.71	16.63	16.60	14.98	14.72	16.02	15.72	12.21	11.67	13.72
TFe ₂ O ₃	11.17	10.35	12.36	11.31	10.62	10.90	11.33	12.78	13.27	11.55	12.31	12.54	11.13	12.85	14.89	15.84	13.68	13.78	1.03	1.09	1.37
MnO	0.14	0.14	0.14	0.19	0.12	0.13	0.20	0.17	0.21	0.14	0.17	0.20	0.20	0.17	0.25	0.21	0.21	0.16	0.05	0.03	0.06
MgO	4.21	4.33	5.21	4.53	3.78	3.41	4.46	5.18	5.91	5.18	5.53	6.05	9.67	7.51	6.12	8.24	5.60	4.65	0.20	0.15	0.29
CaO	18.25	19.43	9.69	6.07	6.48	5.98	4.97	12.49	11.59	11.16	12.87	9.65	8.33	9.10	11.97	10.08	8.61	10.72	0.40	0.34	0.63
Na ₂ O	1.40	1.59	4.09	5.02	5.10	6.01	5.59	3.60	3.73	2.73	3.46	3.99	3.85	3.92	3.68	3.03	3.91	3.45	3.26	3.45	4.62
K ₂ O	0.16	0.39	1.06	1.75	1.37	1.51	1.77	0.43	0.29	0.21	0.24	0.43	0.19	0.15	0.23	0.48	0.56	0.55	5.20	5.08	4.86
P ₂ O ₅	0.40	0.42	0.46	0.65	0.61	0.65	0.29	0.33	0.31	0.37	0.32	0.31	0.30	0.54	0.58	0.63	0.65	0.03	0.04	0.06	
LOI	4.95	6.78	4.95	2.42	2.63	1.8	2.34	6.76	6.57	6.64	6.68	4.97	4.93	4.79	6.72	2.41	2.43	0.76	0.88	1.25	
Mg# ^a	45	48	48	47	44	41	46	47	50	50	50	52	66	56	47	53	47	43	30	23	32
Li	39.4	36.2	44.8	16.2	13.5	8.69	19.3	12.7	16.1	13.4	14.5	16	36.6	26.3	20.9	19.2	21.4	8.35	39.1	38.1	37
Sc	23.2	27.8	28.1	25.3	20.8	23.8	26.1	25.1	23.2	27.3	28.4	25.6	26.1	25.9	22.6	25	25.8	27.4	2.47	2.52	3.17
V	260	257	247	246	236	220	267	218	232	239	275	219	218	210	308	339	320	348	2.43	2.75	5.72
Cr	236	226	271	36	39.3	31.4	31.8	147	146	143	131	132	229	220	146	143	121	124	0.75	0.92	0.71
Co	35.7	33.9	39.1	30.6	26.4	29.1	29.9	38.6	37	41.8	40.4	41.8	54.1	45.7	43	41.5	37.3	41.3	0.47	0.56	0.65
Ni	105	100	121	18.1	25	17	18.5	69.5	75.5	64.9	59.5	65.7	106	106	90.3	85.2	71.6	74.8	0.27	0.38	1.15
Cu	23.9	24.1	61.3	25.5	25.3	16.3	8.36	30.2	20.5	12.7	21.7	15.8	23	22.1	55.2	70.8	38.1	55.9	1.7	2.45	2.02
Zn	71.5	70.2	89.3	122	120	114	125	80.7	92.8	82	87.6	85.5	89.9	83.8	124	108	119	126	34.5	29.4	51.4
Ga	22.1	23.9	18.5	21.7	22.6	21.4	24.9	16.3	16.9	16.6	17.9	17.6	17.3	17.9	18	20.8	22.5	9.16	7.97	12.9	
Rb	0.57	7.24	24.1	22.9	18	17.2	27.2	3.33	2.52	1.13	1.5	3.52	1.15	0.99	3.35	6.53	5.45	5.31	126	118	103
Sr	114	148	354	509	418	240	328	594	511	480	588	671	680	689	514	315	541	488	77.6	56.3	79.3
Y	24.8	28.7	30.3	52.5	54	51.7	56.3	25.7	27.7	27	32.4	28	27.9	26.6	31.3	34.7	39.4	41	24	26.5	30
Zr	234	275	232	433	394	419	462	217	241	226	249	250	232	207	244	279	308	299	192	210	259
Nb	4.68	4.91	5.28	14.9	14.5	14.5	15.9	5.09	5.58	5.23	6.22	5.69	5.32	5.06	6.49	7.26	7.8	8.47	5.98	6.61	7.15
Cs	0.21	0.83	2.57	0.37	0.29	0.49	0.4	0.75	0.57	0.94	0.59	0.77	0.94	1.09	0.2	0.31	0.12	0.059	4.35	3.26	4.15
Ba	26.5	45.9	83.4	338	230	360	597	72.3	66.7	54.1	67.5	83.4	89.3	76.5	44.2	65.1	332	205	1053	987	879
La	10.5	11.4	12.4	23.6	24	22.7	25.2	9.51	10.4	10	12	10.6	9.04	8.7	13.2	14.7	17.3	18	20.8	22.5	23.1
Ce	27.5	29.8	32	60.1	61.9	58.7	63.9	24.4	26.3	25.6	30	27.1	23.9	22.9	32.9	36.5	41.9	44.4	42.9	46.4	49.4
Pr	4.1	4.46	4.78	8.61	8.75	8.41	9.16	3.59	3.89	3.85	4.56	4.04	3.62	3.5	4.67	5.19	5.97	6.36	4.97	5.47	6.2
Nd	17.9	19.5	20.9	36.1	36.9	35.3	38.2	15.8	17	16.9	19.9	17.6	16.3	15.5	22.3	24.9	29.1	30.2	17.5	19.6	22.7
Sm	4.73	5.16	5.51	9.73	10.1	9.43	10.3	4.35	4.65	4.73	5.54	4.87	4.62	4.43	5.57	5.85	6.76	6.96	3.84	4.26	5.01
Eu	1.43	1.53	1.73	2.24	2.14	2.15	2.39	1.4	1.64	1.5	1.67	1.53	1.51	1.46	1.84	2.11	2.36	2.39	1.13	1.22	1.3
Gd	3.62	3.95	4.16	7.51	7.72	7.21	7.95	3.29	3.56	3.59	4.22	3.66	3.49	3.33	5.51	6.37	7.12	7.04	3.23	3.6	4.13
Tb	0.75	0.81	0.86	1.55	1.6	1.5	1.64	0.7	0.76	0.76	0.9	0.79	0.76	0.73	1.01	1.09	1.24	1.33	0.59	0.66	0.77
Dy	4.34	4.67	4.96	8.85	9.15	8.66	9.43	4.18	4.42	4.47	5.22	4.63	4.55	4.36	6.01	6.55	7.51	7.97	3.3	3.64	4.24
Ho	0.9	0.99	1.04	1.83	1.88	1.78	1.93	0.88	0.94	0.93	1.1	0.98	0.94	0.91	1.16	1.25	1.45	1.52	0.72	0.8	0.91
Er	2.33	2.54	2.68	4.63	4.78	4.51	4.93	2.26	2.41	2.38	2.81	2.52	2.44	2.35	3.43	3.94	4.3	4.5	2.04	2.28	2.59
Tm	0.44	0.47	0.5	0.85	0.87	0.83	0.9	0.42	0.45	0.45	0.53	0.47	0.46	0.44	0.52	0.6	0.64	0.71	0.42	0.45	0.51
Yb	2.32	2.52	2.68	4.48	4.7	4.33	4.77	2.24	2.39	2.35	2.8	2.5	2.45	2.31	3.18	3.6	4.15	4.33	2.31	2.55	2.84
Lu	0.32	0.35	0.37	0.6	0.62	0.57	0.64	0.31	0.33	0.32	0.38	0.35	0.34	0.31	0.51	0.55	0.64	0.67	0.33	0.36	0.4
Hf	5.46	5.86	6.07	10.40	10.20	10.20	11.10	5.04	5.32	5.28	6.10	5.63	5.31	4.93	6.14	7.31	8.60	8.40	5.65	6.14	7.17
Ta	0.35	0.38	0.39	1.08	1.09	1.04	1.15	0.56	0.48	0.43	0.51	0.46	0.42	0.41	0.40	0.46	0.48	0.51	0.59	0.66	0.69
Pb	4.24	4.01	4.05	7.58	10.20	7.38	7.93	1.93	2.26	1.90	2.21	1.98	1.70	1.96	3.03	3.01	4.14	4.07	19.50	20.20	22.80
Th	0.52	0.62	0.67	2.47	2.93	2.44	2.68	0.40	0.43	0.41	0.50	0.45	0.38	0.36	0.61	0.69	0.76	0.79	8.72	9.69	9.94
U	0.20	0.26	0.23	0.51	0.50	0.42	0.65	0.17	0.21	0.19	0.25	0.13	0.22	0.13	0.23	0.27	0.27	1.78	2.17	2.48	
ΣREE	81	88	95	171	175	166	181	73	79	78	92	82	74	71	102	113	130	136	104	114	124
(La/Yb)N	3.25	3.24	3.32	3.78	3.66	3.76	3.79	3.05	3.12	3.05	3.07	3.04	2.65	2.70	2.98	2.99	2.98	6.			

4. Analytical methods

In order to determine the nature and evolution of the western Luliang Uplift, representative volcanic rocks collected from the boreholes in the Xiayan High were selected for the analysis of major and trace elements and whole rock Sr–Nd isotope, zircon SIMS U–Pb dating and in-situ Lu–Hf isotope.

4.1. Zircon SIMS U–Pb dating

Zircon grains in the dacite of well MD4 were separated for SIMS studies using conventional heavy liquid and magnetic techniques. Representative grains were handpicked using a binocular microscope, mounted in an epoxy resin disk, and then polished and coated with a gold film. The grains were documented under transmitted and reflected light micrographs as well as cathodoluminescence (CL) images to reveal their internal structures, and the mount was vacuum-coated with high purity gold prior to secondary ion mass spectrometry (SIMS) analysis. Measurements of U, Th and Pb were conducted using a Cameca IMS-1280 SIMS. U–Th–Pb ratios and absolute abundances were determined relative to the standard zircon 91500 (Wiedenbeck et al., 1995), analyses of which were interspersed with those of unknown grains, using operating and data processing procedures similar to those described by Li et al. (2009). A long-term uncertainty of 1.5% (1 RSD) for $^{206}\text{Pb}/^{238}\text{U}$ measurements of the standard zircons was propagated to the unknowns (Li et al., 2010), despite that the measured $^{206}\text{Pb}/^{238}\text{U}$ error in a specific session is generally around 1% (1 RSD) or less. Measured compositions were corrected for common Pb using non-radiogenic ^{204}Pb . Corrections are sufficiently small to be insensitive to the choice of common Pb composition, and an average of present-day crustal composition (Stacey and Kramers, 1975) is used for the common Pb assuming that the common Pb is largely surface contamination introduced during sample preparation. Uncertainties on individual analyses in data tables are reported at a 1 σ level; mean ages for pooled U/Pb (and Pb/Pb) analyses are quoted with 95% confidence interval. Data reduction was carried out using the Isoplot/Ex v. 2.49 program (Ludwig, 2001).

4.2. Major and trace element analyses

Major and trace elements of all the samples were carried out in the Analytical Laboratory of the Beijing Research Institute of Uranium Geology. Major elements were analyzed by a Philips PW2404 X-ray fluorescence spectrometer (XRF). Trace element data were obtained using a Finnigan MAT high resolution inductively coupled plasma mass spectrometer (HR-ICPMS). The precision and accuracy of the ICP-MS and X-ray fluorescence data were reported by Cullen et al. (2001) and Wu et al. (2010), respectively.

4.3. The whole rock Sr–Nd analyses

Sr–Nd isotopic data of volcanic rocks were performed in Beijing at the Institute of Geology and Geophysics, Chinese Academy of Sciences, using a multicollector VG 354 mass spectrometer in static mode. Approximately 100–150 mg of whole-rock powder was decomposed in a mixture of HF-HClO₄ in screw-top Teflon beakers, and Rb, Sr, Sm and Nd were separated by cation exchange columns, following the procedure of Zhang et al. (2001). Rb, Sr, Sm and Nd concentrations were determined by isotope dilution method, using a mixed ^{87}Rb - ^{84}Sr - ^{149}Sm - ^{150}Nd spike solution. Procedural blanks were less than 200 pg for Sr and less than 50 pg for Nd. $^{143}\text{Nd}/^{144}\text{Nd}$ ratios were normalized to $^{146}\text{Nd}/^{144}\text{Nd}$ (0.7219) and $^{87}\text{Sr}/^{86}\text{Sr}$ ratios were normalized to $^{86}\text{Sr}/^{88}\text{Sr}$ (0.1194). Detailed analytical procedures were described in Chen et al. (2002). During the course of this study, standards NBS 607 and BCR-1 gave $^{87}\text{Sr}/^{86}\text{Sr}$ ratios of 1.20032 ± 28 (2σ) and $^{143}\text{Nd}/^{144}\text{Nd}$ ratios of 0.512626 ± 9 (2σ), respectively. Analytical

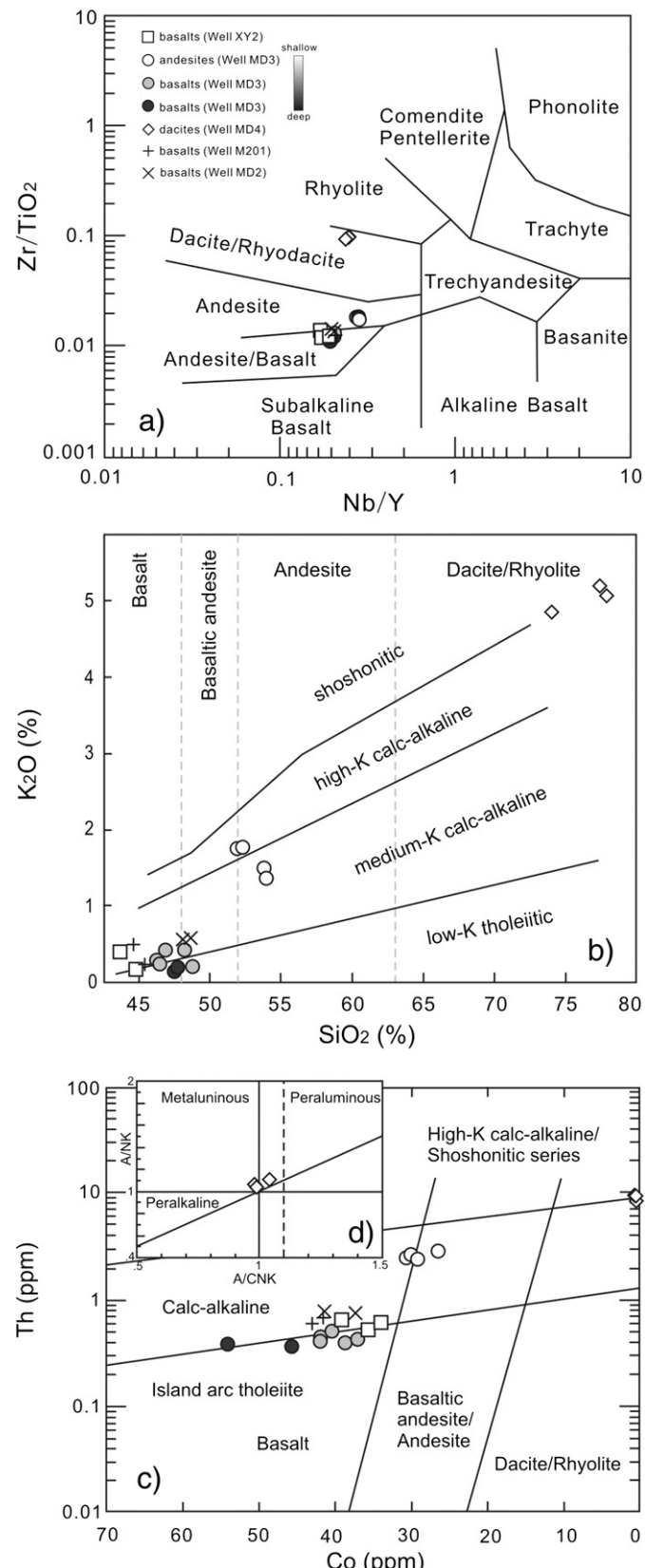


Fig. 6. Geochemical classification diagrams for the Early Carboniferous volcanic rocks in the western Luliang Uplift. (a) Zr/TiO_2 versus Nb/Y diagram (after Winchester and Floyd (1977)), (b) K_2O versus SiO_2 diagram, (c) Th versus Co diagram (after Hastie et al. (2007)) and (d) A/NK versus A/CNK diagram (after Maniar and Piccoli (1989)).

precision is ~1% for $^{87}\text{Rb}/^{86}\text{Sr}$ and 0.5% for $^{147}\text{Sm}/^{144}\text{Nd}$, respectively. The depleted mantle Nd model ages were calculated using the present-day depleted mantle $^{143}\text{Nd}/^{144}\text{Nd}$ and $^{147}\text{Sm}/^{144}\text{Nd}$ values of 0.513151 and 0.21357, an average crustal $^{147}\text{Sm}/^{144}\text{Nd}$ ratio of 0.118 (Jahn and Condie, 1995), and the rock formation ages. The Rb–Sr and Sm–Nd isotopic compositions of samples from the samples are presented in Table 3.

4.4. In-situ Lu–Hf isotopic analyses

In-situ zircon Hf isotopic analyses of dacite from well MD4 were conducted using a Neptune MC-ICPMS, equipped with a 193 nm laser, at the State Key Laboratory of Continental Dynamics in Northwest University, Xi'an. During the analyses, a laser repetition rate of 10 Hz at 100 mJ was used and spot sizes were either 32 or 63 μm . Raw count rates for ^{172}Yb , ^{173}Yb , ^{175}Lu , $^{176}(\text{Hf} + \text{Yb} + \text{Lu})$, ^{177}Hf , ^{178}Hf , ^{179}Hf , ^{180}Hf and ^{182}W were collected and isobaric interference corrections for ^{176}Lu and ^{176}Yb on ^{176}Hf need to be precisely determined. ^{176}Lu was calibrated using the ^{175}Lu value and a correction was made for ^{176}Hf . A $^{176}\text{Yb}/^{172}\text{Yb}$ of 0.5887 and the mean of Yb obtained during the Hf analysis on the same spot was applied for the interference correction of ^{176}Yb on ^{176}Hf (Iizuka and Hirata, 2005). During the analyses, $^{176}\text{Hf}/^{177}\text{Hf}$ and $^{176}\text{Lu}/^{177}\text{Hf}$ ratios of the standard zircon (91500) were 0.282294 ± 15 (2σ , $n = 20$) and 0.00031, similar to the commonly accepted $^{176}\text{Hf}/^{177}\text{Hf}$ ratio of 0.282302 ± 8 and 0.282306 ± 8 (2σ) measured using solution method (Goolaerts et al., 2004). The notations

of $\varepsilon_{\text{Hf}}(t)$, $f_{\text{Lu/Hf}}$, T_{DM} are defined as the same to those in Yang et al. (2007), with interpretations of single-stage Hf model ages for positive $\varepsilon_{\text{Hf}}(t)$ values.

5. Analytical results

5.1. Zircon U–Pb dating results

The zircon U–Pb data are summarized in Table 1 and presented in concordia diagrams in Fig. 5. Zircon grains separated from the Carboniferous dacite at a depth of 3449.5 m from well MD4 are light brown or colorless, transparent to translucent, and occur as euhedral, stubby to prismatic crystals, generally 80–120 μm in length, with length to width ratio of around 2.0. The cathodoluminescence (CL) images show that all of the grains possess good oscillatory zoning and lack visible inherited cores (Fig. 5a). Twenty zircon grains were analyzed from the dacite (sample J11-5-1), and the results show a wide range in U (88–553 ppm) and Th (53–942 ppm) contents, with Th/U ratios between 0.5 and 1.7 (Table 1). In contrast to metamorphic zircons whose Th/U ratios are generally lower than 0.1 (Ubatto, 2002), the zircons from this study are characteristic of magmatic origin as also confirmed by the typical oscillatory zoning resulting from magmatic crystallization (Hartmann and Santos, 2004). Zircons from the dacite yielded $^{206}\text{Pb}/^{238}\text{U}$ ages ranging from 309 ± 4.6 Ma to 340 ± 5.0 Ma with a weighted mean age of 326.6 ± 2.8 Ma (MSWD = 0.079) (Fig. 5b). In view of the well-developed crystal faces and magmatic

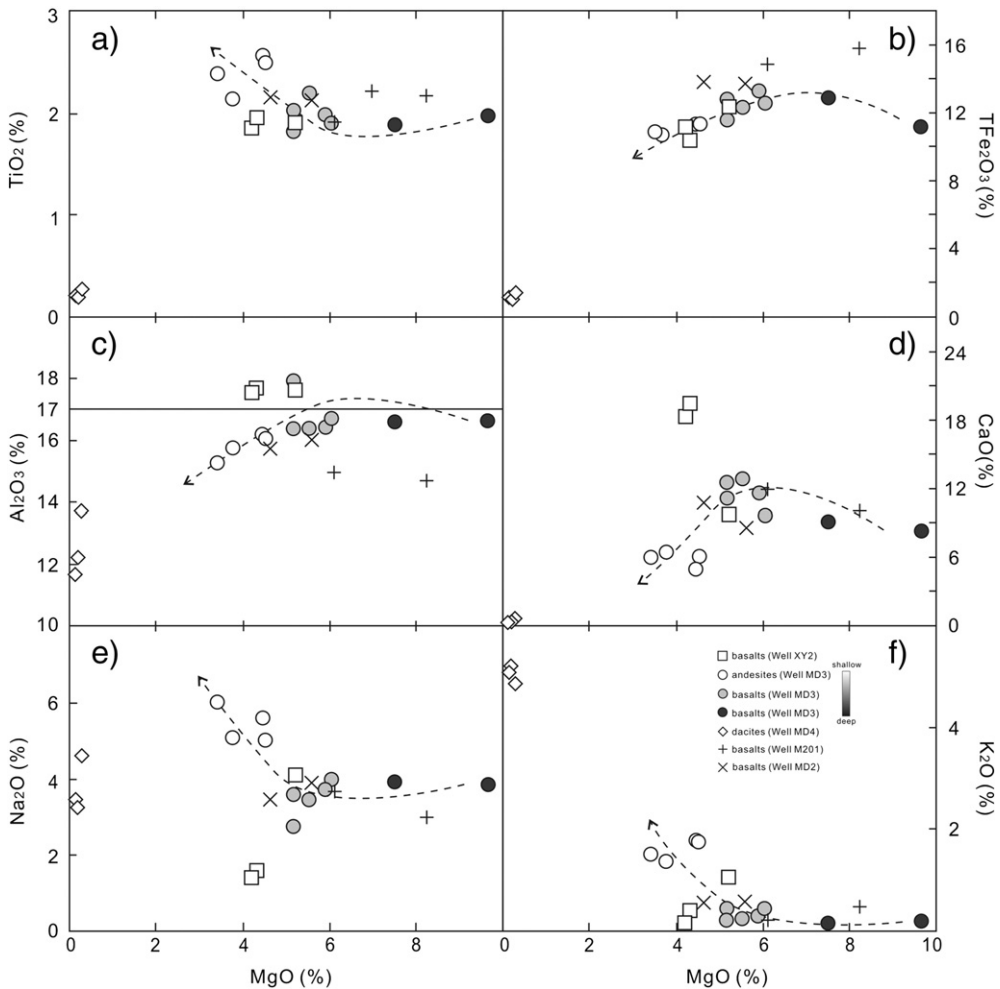


Fig. 7. Major elements TiO_2 (a), Fe_2O_3 (b), Al_2O_3 (c), CaO (d), Na_2O (e) and K_2O (f) versus MgO for the Early Carboniferous volcanic rocks in the western Luliang Uplift.

oscillatory zoning, the $^{206}\text{Pb}/^{238}\text{U}$ mean age of 326.6 ± 2.8 Ma is interpreted as the time of crystallization of the dacite, which is consistent with the reported Rb-Sr age of the basalt from well XY2 (323 Ma, Wang et al., 2002).

5.2. Major oxides and trace elements

All the major oxides were LOI-free normalized before petrogenetic interpretation because of high loss on ignition (LOI) ranging from 0.76 to 6.78% (Table 2), suggesting that these samples were likely affected by alteration. In general, the transition metals (e.g., Cr and Ni) and HFSEs (e.g., Ti, Zr, Y, Nb and REE) in the rocks are relatively immobile under conditions of low-temperature alteration (Pearce and Cann, 1973; Winchester and Floyd, 1977), and are usually used to discuss the classification and original characteristics for volcanic rocks (Frey et al., 2002).

The basalts and basaltic andesites have low SiO_2 contents (43.69–53.99%) and total alkalis, and medium to high Al_2O_3 contents (14.72–17.92%). They contain variable concentrations of TiO_2 (1.81–2.56%) and low contents of MgO (3.41–9.67%), with $\text{Mg}^{\#}$ ($\text{Mg}^{\#} = \text{molar Mg}/(\text{Mg} + \text{Fe})$) ranging from 30 to 66. The dacites are predominantly characterized by moderate alkali concentrations ($\text{K}_2\text{O} + \text{Na}_2\text{O} = 8.46\text{--}9.48\%$) and high SiO_2 contents, ranging from 74.12–77.95%. In the Zr/TiO_2 versus Nb/Y diagram (Fig. 6a), the rocks plot in the basalt, andesite and dacite/rhyodacite fields, showing a wide variation from low-K tholeiitic to shoshonitic series (Fig. 6b). In the Th versus Co diagram (Fig. 6c), the basalts plot mainly in the island arc tholeiitic to calc-alkaline series fields, and the basaltic andesites fall in the calc-alkaline series fields, whereas the dacites plot in the calc-alkaline to high-k calc-alkaline series. The relative low aluminum contents (11.67–13.72%) and A/CNK (molar $\text{Al}_2\text{O}_3/(\text{CaO} + \text{Na}_2\text{O} + \text{K}_2\text{O})$) values of 0.98 to 1.04, together with the lack of alkaline mafic or peraluminous minerals, indicate that these dacites belong to metaluminous or slightly aluminous I-type granitoid series (Fig. 6d). These mafic to felsic volcanic rocks show little or no correlation on the MgO versus major oxides diagrams (Fig. 7). All these rocks exhibit coherent chondrite-normalized REE patterns, characterized by relative enrichment of light rare earth elements (LREE, $(\text{La/Yb})_{\text{N}} = 2.65\text{--}6.46$) and near flat heavy rare earth (HREE, $(\text{Gd/Yb})_{\text{N}} = 1.16\text{--}1.46$) segments, with weak or no Eu anomalies ($\text{Eu}^*/\text{Eu} = 0.74\text{--}1.23$, Fig. 8a, c and e). They also have similar N-MORB normalized trace element patterns, characterized by pronounced negative Nb and Ta anomalies and variable enrichment in large ion lithophile elements (LILE, Rb, Ba, Th and U) (Fig. 8b, d and f).

5.3. Whole rock Sr-Nd isotope compositions

Five basaltic rocks and one dacite sample from the three boreholes (wells XY2, MD3 and MD4) in the Xiayan High were chosen for Sr-Nd isotopes analyses. Their Sr-Nd isotopic compositions are listed in Table 3. The initial $^{87}\text{Sr}/^{86}\text{Sr}$ ratios and $\varepsilon_{\text{Nd}}(t)$ values were calculated at 327 Ma on the basis of zircon SIMS U-Pb dating. The Sr-Nd isotope data are plotted in terms of initial $^{87}\text{Sr}/^{86}\text{Sr}$ ratios versus $\varepsilon_{\text{Nd}}(t)$ values (Fig. 9a), and compared with the reported compositional fields of the Early Carboniferous volcanic rocks in the West Junggar terrane (Fig. 9a, b) (Geng et al., 2011). All samples exhibit a narrow range in their $^{143}\text{Nd}/^{144}\text{Nd}$ and $^{87}\text{Sr}/^{86}\text{Sr}$ ratios (Table 3). Initial $^{87}\text{Sr}/^{86}\text{Sr}$ ratios of the basaltic rocks in this study range from 0.703497 to 0.704826, and their initial Nd isotopes exhibit minor variation between 0.512896 and 0.512991 and $\varepsilon_{\text{Nd}}(t)$ from 6.4 to 8.0. The Nd model ages (T_{DM}) are ranging between 573 and 763 Ma (Table 3). Initial $^{87}\text{Sr}/^{86}\text{Sr}$ ratios of the dacites vary from 0.701625 to 0.701633, and the Nd isotopes ranged from 0.512742 to 0.512750, $\varepsilon_{\text{Nd}}(t)$ from 4.8 to 4.9. Their Nd model ages (T_{DM}) show similar variations from 741 to 756 Ma. All the basaltic rocks have young Nd model age and plot close to the mantle array and within the field of Early Carboniferous volcanic rocks in the West

Table 3
Whole-rock Sr-Nd isotopic compositions of the Early Carboniferous volcanic rocks from the western Luliang Uplift.

Well	Sample	Rock	Rb(ppm)	Sr(ppm)	$^{87}\text{Rb}/^{86}\text{Sr}$	$^{87}\text{Sr}/^{86}\text{Sr}$	2σ	$(^{87}\text{Sr}/^{86}\text{Sr})_i$	Sm(ppm)	Nd(ppm)	$^{143}\text{Nd}/^{144}\text{Nd}$	$^{147}\text{Sm}/^{144}\text{Nd}$	2σ	$\varepsilon_{\text{Nd}}(t)$	$T_{\text{DM}}(\text{Ma})$
XY2	J11-2-1	Basalt	0.57	114	0.014411	0.704881	0.000018	0.704826	4.73	17.9	0.159763	0.512919	0.000011	7.0	653
MD3	J11-3-1	Basaltic andesite	22.9	509	0.130129	0.704678	0.000013	0.704178	9.73	36.1	0.162956	0.512896	0.000011	6.4	763
MD3	J11-3-1R	Basaltic andesite	22.9	509	0.130129	0.704679	0.000013	0.704179	9.73	36.1	0.162957	0.512907	0.000011	6.7	730
MD3	J11-3-5	Basalt	3.33	594	0.016213	0.703586	0.000014	0.703524	4.35	15.8	0.166438	0.512961	0.000012	7.6	610
MD3	J11-3-5R	Basalt	3.33	594	0.016213	0.703586	0.000014	0.703524	4.35	15.8	0.166457	0.512940	0.000012	7.2	678
MD3	J11-3-7	Basalt	1.28	542	0.006830	0.703567	0.000011	0.703541	5.28	19.1	0.167137	0.512971	0.000011	7.7	587
MD3	J11-3-12	Basalt	1.15	680	0.004891	0.703516	0.000013	0.703497	4.62	16.3	0.171368	0.512991	0.000013	8.0	573
MD4	J11-5-2	Dacite	118	56.3	6.074237	0.724966	0.000014	0.701633	4.26	19.6	0.131403	0.512750	0.000006	4.9	741
MD4	J11-5-2R	Dacite	118	56.3	6.074233	0.724958	0.000014	0.701625	4.26	19.6	0.131402	0.512742	0.000006	4.8	756

$^{87}\text{Rb}/^{86}\text{Sr}$ and $^{147}\text{Sm}/^{144}\text{Nd}$ ratios were calculated using $\text{Rb}, \text{Sr}, \text{Sm}$ and Nd contents, measured by ICP-MS.

$\varepsilon_{\text{Nd}}(t)$ values were calculated using present-day $(^{147}\text{Sm}/^{144}\text{Nd})_{\text{CHUR}} = 0.1967$ and $(^{143}\text{Nd}/^{144}\text{Nd})_{\text{CHUR}} = 0.512638$.

T_{DM} values were calculated using present-day $(^{147}\text{Sm}/^{144}\text{Nd})_{\text{DM}} = 0.2137$ and $(^{143}\text{Nd}/^{144}\text{Nd})_{\text{DM}} = 0.51315$.

R represents the retested samples.

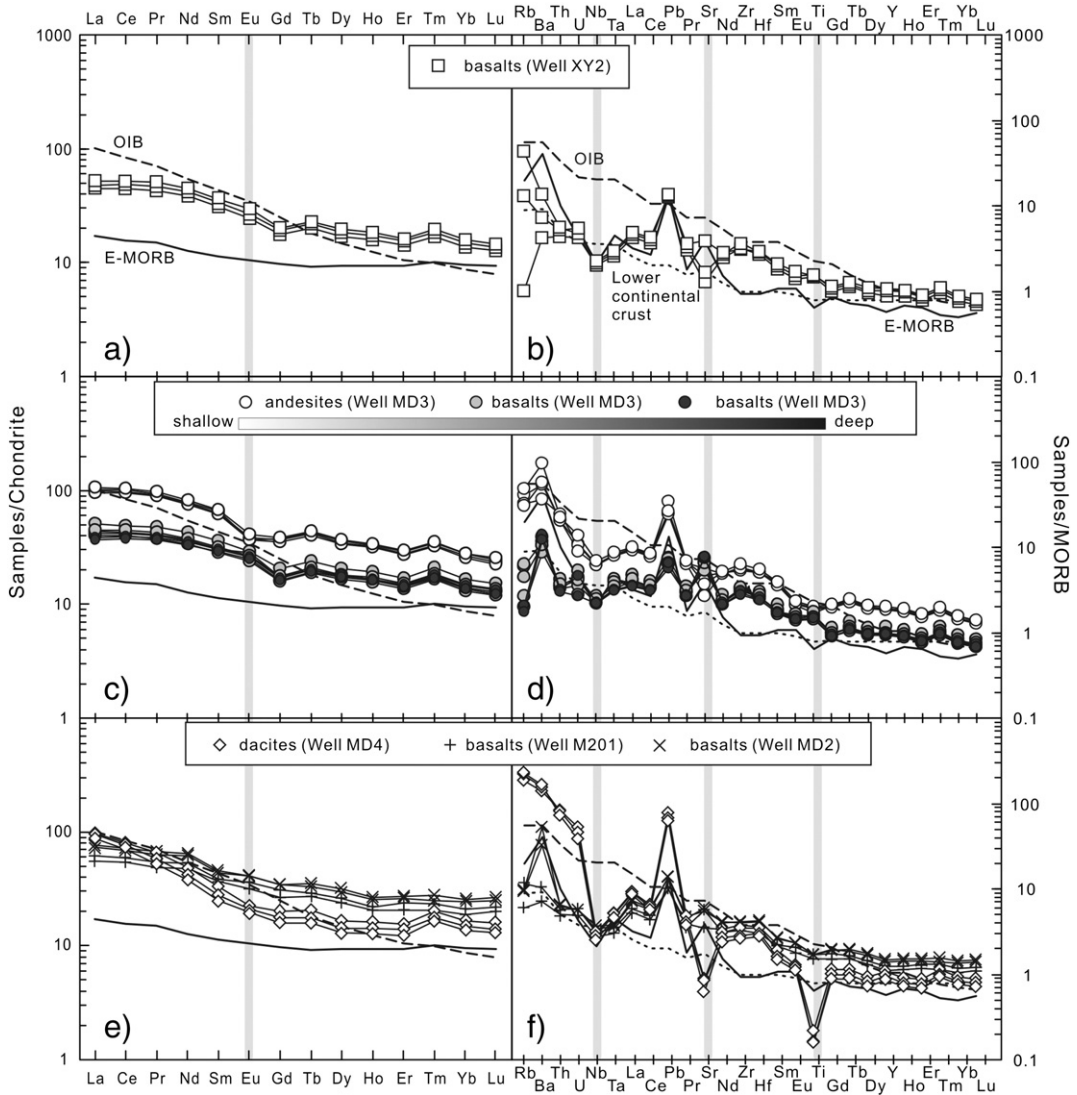


Fig. 8. Chondrite normalized REE patterns and N-MORB normalized trace element spider diagrams for the Early Carboniferous volcanic rocks in the western Luliang Uplift. OIB, E-MORB, N-MORB and chondrite normalized values according to Sun and McDonough (1989). The data on lower continental crust are from Rudnick and Gao (2003).

Junggar terrane (Fig. 9a). In contrast, the dacite shows different Sr–Nd isotopic composition with those of basaltic rocks, indicating that they may be derived from distinct source.

5.4. In-situ zircon Lu–Hf isotope compositions

Nineteen zircon grains from the dacite sample (J11-5-1), whose SIMS U–Pb age has been determined as 326.6 Ma, were analyzed for in-situ Hf isotopic composition by LA-MC-ICPMS method. The analytical data are given in Table 4. The analyzed zircon grains show low $^{176}\text{Lu}/^{177}\text{Hf}$ ratios (0.001598 to 0.003681) with an average value at 0.002672, suggesting a limited radiogenic Hf production over the ~327 Ma lifetimes for these zircons. All the zircons display a narrow variation in initial $^{176}\text{Hf}/^{177}\text{Hf}$ ratios (0.282706 to 0.282858) and $\epsilon_{\text{Hf}}(t)$ values from 4.1 to 9.8 (Table 4). The single-stage Hf isotopic model ages ($T_{\text{DM}1}$) for these nineteen zircons mainly range from 636 to 927 Ma, similar to their $T_{\text{DM}2}$ model ages (574–826 Ma). These ~327 Ma zircons from the dacite have positive $\epsilon_{\text{Hf}}(t)$ values, and plot below the depleted mantle evolution line close to those of the Paleozoic volcanic rocks from the Junggar terrane (Xiao et al., 2011; Su et al., 2012; He et al., 2013; Li et al., 2014 and reference therein) (Fig. 9c).

6. Discussion

6.1. Early Carboniferous northward subduction-related basin system

Multiple sets of sedimentary rocks (e.g., sandstone and mudstone) are involved in the Carboniferous strata, suggesting that the western Luliang Uplift had entered the basin evolution stage in the Carboniferous. The Carboniferous strata of the Xiayan High that is located in the southern part of western Luliang Uplift are characterized by interbedded volcanic and sedimentary rocks, whereas the Yingxi Sag of western Luliang Uplift contains thick Carboniferous volcano-sedimentary sequences and is bounded by faults (e.g. F2 and F3) at its northern side (Fig. 2). Although the Middle Permian to Jurassic strong compression gave rise to thrust faults (F1 and F2) and resulted in the uplift and erosion in the western Luliang Uplift, the thickness of the Carboniferous strata in the hanging wall of F3 becomes larger toward the fault surface, suggesting that the western Luliang Uplift was in an extensional tectonic environment during this period (Fig. 2). The presence of abundant coeval volcanic rocks in the basin provides better insight on the geodynamic mechanism of this extensional basin (Clift et al., 2000; McCann and Saintot, 2003; Draut and Clift, 2006; Leeder, 2011).

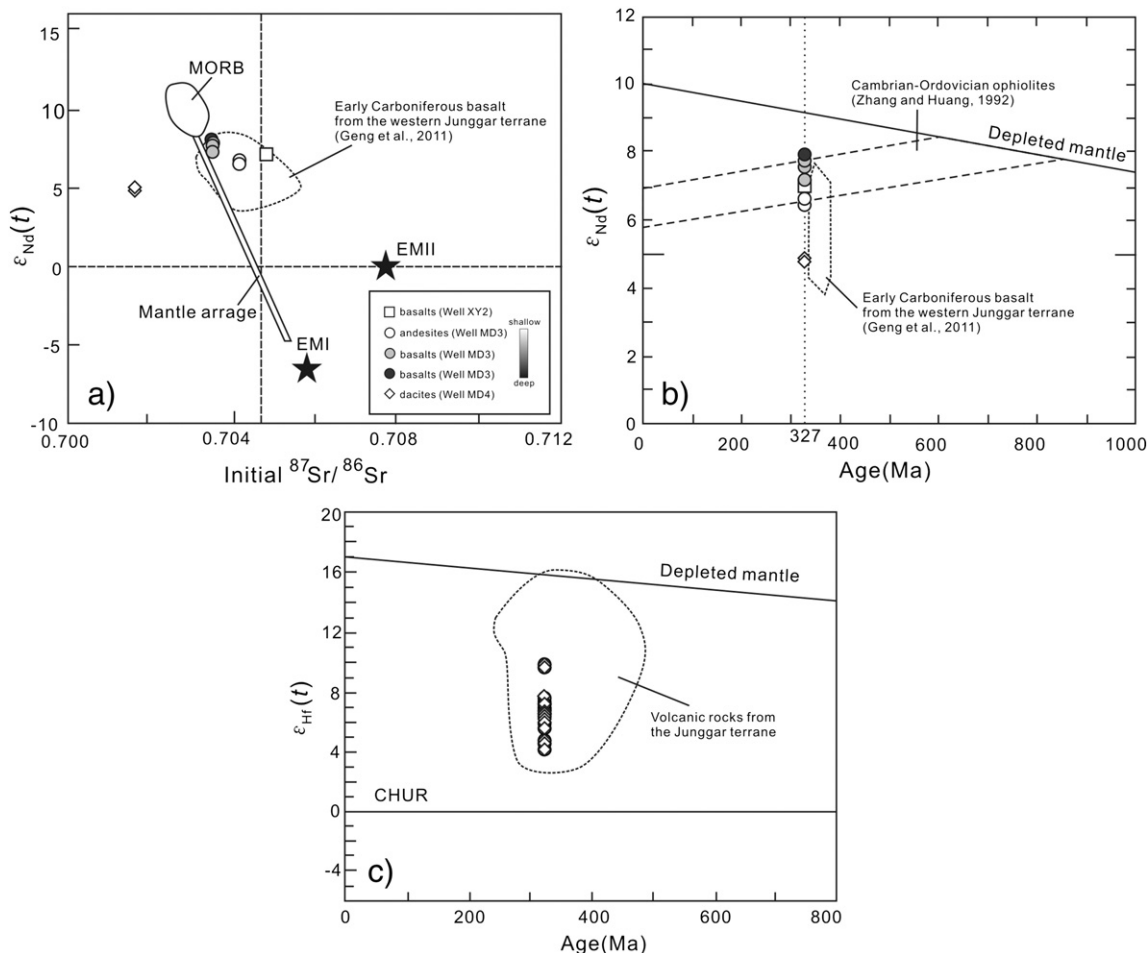


Fig. 9. Plots of $\varepsilon_{\text{Nd}}(t)$ values versus initial $^{87}\text{Sr}/^{86}\text{Sr}$ (a) and age (b) of the Early Carboniferous volcanic rocks in the western Luliang Uplift and zircon Hf isotopic compositions of the dacite (c). The compared data for the Early Carboniferous basalts from the West Junggar terrane are from Geng et al. (2011). Data for the Cambrian-Ordovician ophiolites are from Zhang and Huang (1992), and the enriched mantle EMI and EMII members (Hart, 1988) are shown for comparison.

Table 4
Lu-Hf isotope analysis results of zircons for the Early Carboniferous dacite from the western Luliang Uplift.

Spots	Age(Ma)	$^{176}\text{Yb}/^{177}\text{Hf}$	$^{176}\text{Lu}/^{177}\text{Hf}$	$^{176}\text{Hf}/^{177}\text{Hf}$	$\pm 2\sigma$	$\varepsilon_{\text{Hf}}(t)$	$T_{\text{DM1}}(\text{Ma})$	$T_{\text{DM2}}(\text{Ma})$	$f_{\text{Lu/Hf}}$
J11-5-1@01	326.6	0.081834	0.003270	0.282780	0.000022	6.7	712	792	-0.90
J11-5-1@02	326.6	0.062596	0.002507	0.282779	0.000018	6.9	699	786	-0.92
J11-5-1@03	326.6	0.070055	0.002667	0.282749	0.000014	5.8	746	841	-0.92
J11-5-1@04	326.6	0.071095	0.002757	0.282778	0.000024	6.8	704	789	-0.92
J11-5-1@05	326.6	0.094284	0.003627	0.282724	0.000016	4.7	805	898	-0.89
J11-5-1@07	326.6	0.039342	0.001598	0.282850	0.000014	9.6	578	645	-0.95
J11-5-1@08	326.6	0.065666	0.002589	0.282768	0.000020	6.5	716	806	-0.92
J11-5-1@09	326.6	0.089881	0.003422	0.282706	0.000020	4.1	826	927	-0.90
J11-5-1@10	326.6	0.058037	0.002356	0.282788	0.000020	7.2	683	768	-0.93
J11-5-1@11	326.6	0.093723	0.003681	0.282748	0.000026	5.6	768	853	-0.89
J11-5-1@12	326.6	0.079898	0.003135	0.282765	0.000018	6.3	731	817	-0.91
J11-5-1@13	326.6	0.081765	0.003150	0.282715	0.000020	4.5	807	908	-0.91
J11-5-1@14	326.6	0.062732	0.002468	0.282767	0.000016	6.5	716	807	-0.93
J11-5-1@15	326.6	0.060004	0.002284	0.282769	0.000022	6.6	708	801	-0.93
J11-5-1@16	326.6	0.051311	0.002070	0.282858	0.000018	9.8	574	636	-0.94
J11-5-1@17	326.6	0.056247	0.002278	0.282786	0.000016	7.2	684	770	-0.93
J11-5-1@18	326.6	0.064311	0.002513	0.282797	0.000018	7.5	672	753	-0.92
J11-5-1@19	326.6	0.068998	0.002704	0.282776	0.000020	6.7	707	793	-0.92
J11-5-1@20	326.6	0.044579	0.001702	0.282782	0.000018	7.2	679	771	-0.95

^{176}Lu decay constant is $1.865 \times 10^{-11} \text{ yr}^{-1}$.

Chondritic values: $^{176}\text{Lu}/^{177}\text{Hf} = 0.0332 \pm 0.0002$, $^{176}\text{Hf}/^{177}\text{Hf} = 0.282772 \pm 0.000029$.

Depleted mantle values: $(^{176}\text{Lu}/^{177}\text{Hf})_{\text{DM}} = 0.0384$, $(^{176}\text{Hf}/^{177}\text{Hf})_{\text{DM}} = 0.28325$.

$T_{\text{DM1}} = 1/\lambda \times \ln(1 + ((^{176}\text{Hf}/^{177}\text{Hf})_{\text{S,L}} - (^{176}\text{Hf}/^{177}\text{Hf})_{\text{DM}})/((^{176}\text{Lu}/^{177}\text{Hf})_{\text{S,L}} - (^{176}\text{Lu}/^{177}\text{Hf})_{\text{DM}}))$.

$T_{\text{DM2}} = 1/\lambda \times \ln(1 + ((^{176}\text{Hf}/^{177}\text{Hf})_{\text{S,L}} - (^{176}\text{Hf}/^{177}\text{Hf})_{\text{DM,t}})/((^{176}\text{Lu}/^{177}\text{Hf})_{\text{S,L}} - (^{176}\text{Lu}/^{177}\text{Hf})_{\text{DM}})) + t$.

The Early Carboniferous basaltic rocks in the western Luliang Uplift exhibit calc-alkaline and tholeiitic nature, and have low Mg# (41–66) and Cr (31.4–271 ppm) and Ni (17.0–121 ppm) contents, reflecting that the basaltic magmas are not primitive magmas and were possibly produced from variably fractionated melts. In addition, the LILE and LREE enrichment and HFSE depletion suggest a subduction zone origin/arc affinity (Pearce, 1983) or the contribution from crustal contamination. However, these basaltic rocks have low Th/La (0.04–0.12), Th/Ce (0.02–0.04) and La/Sm (1.96–2.59) ratios, indicating that little or no crustal components were involved during the generation of the magmas, which is also supported by the absence of obvious positive Zr-Hf anomalies (Zhao and Zhou, 2007). Their low initial $^{87}\text{Sr}/^{86}\text{Sr}$ ratios (0.703497–0.704826) and positive $\epsilon_{\text{Nd}}(t)$ values (6.4–8.0) reflect that the source had significant contribution from a depleted mantle component. This is also confirmed by the trace element ratios ($\text{Zr/Nb} = 27\text{--}56$, $\text{Zr/Hf} = 36\text{--}50$ and $\text{Nb/Ta} = 9\text{--}17$) which are similar to N-MORB (~30, ~36 and 6–14, respectively, Rollinson, 1993). Relative high Sm/Yb (1.61–2.18) and low La/Yb (1.96–2.59) ratios further suggest the nature of this depleted mantle consisting of garnet peridotite (Fig. 10). Nevertheless, they have lower $\epsilon_{\text{Nd}}(t)$ values than those of MORB (Fig. 9a) and plot in the field between N-MORB and lower crust in the Nb/Th versus Ti/Yb diagram (Fig. 11a). Such features are typically related to supra-subduction setting where the overlying depleted mantle wedge is modified by the addition of materials from the subducting slab (Hawkins, 2003). The enrichment of LILEs and LREE relative to HFSE and HREE and variable Ba/Th (50–439) and Ba/Nb (5.7–42) ratios support the input of fluid components into magma source. In the $(\text{La/Yb})_N$ versus Yb_N diagram (Fig. 12a), all the basaltic rocks plot in the classic island arc field. In contrast, the dacites have low TiO_2 (0.20–0.27%) contents and Mg# (23–32) and exhibit lower Nd isotopic components ($\epsilon_{\text{Nd}}(t) = 4.8\text{--}4.9$) than those mantle-derived basaltic rocks. They display similar Th/La ratios (0.42–0.43) with those of the continental crust (0.3, Plank, 2005). In addition, these samples show positive $\epsilon_{\text{Hf}}(t)$ values (4.1–9.8) and insignificant Eu anomalies, and fall near the granite field in the Ti/Y versus Ti/Zr diagram, suggesting their derivation from crust source (Fig. 11b), indicating that their parental melts possibly originated from partial melting of a juvenile lower crustal source without plagioclase in the residue (Sen and Dunn, 1994). The dacites exhibit low ACNK (0.98–1.04) and Ga/Al ratios and are enriched in LILEs and depleted in HFSEs with Nb, Ta and Ti anomalies, and show I-type granite affinity. Also, they have typical feature of volcanic arc granites with low Ta (0.59–0.69 ppm) and Yb (0.31–2.84 ppm) contents, indicating their formation in a subduction-related environment (Fig. 12b).

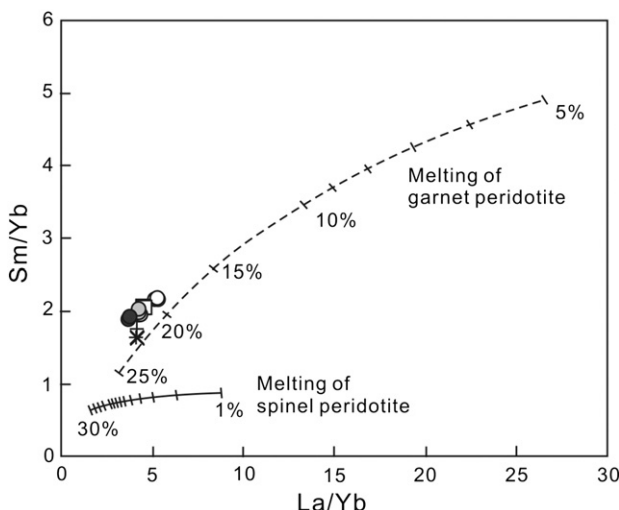


Fig. 10. Plots of Sm/Yb versus La/Yb for the Early Carboniferous basaltic rocks from the western Luliang Uplift. Also shown are batch melting curves for garnet peridotite and spinel peridotite, with partition coefficients from Johnson et al. (1990).

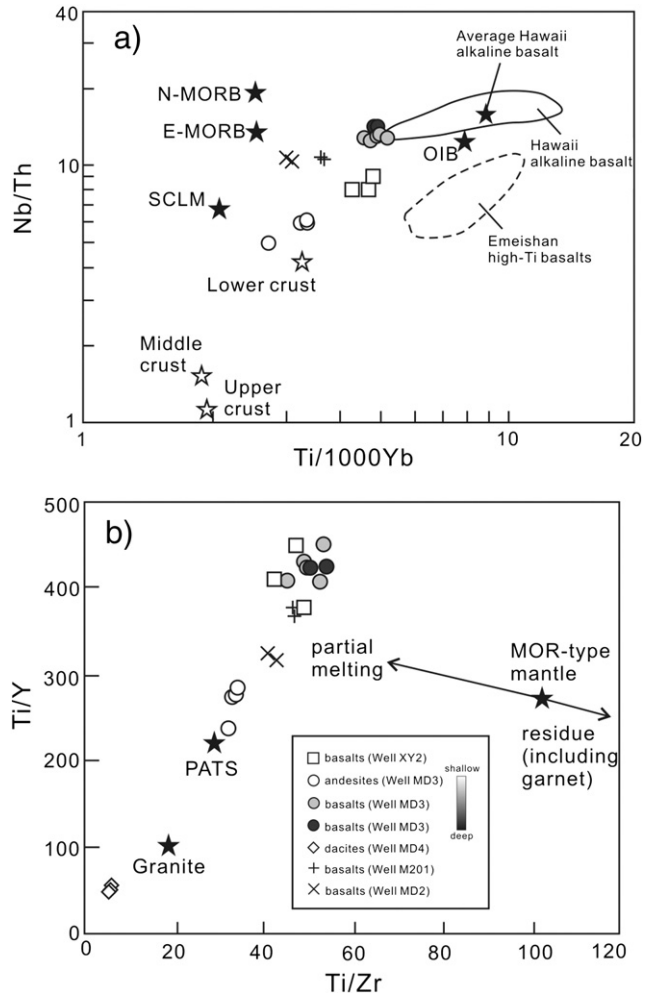


Fig. 11. (a) Nb/Th versus Ti/1000Yb diagram. Data shown for comparison on N-MORB, SCLM (sub-continental lithospheric mantle) and crustal components are from Sun and McDonough (1989), McDonough (1990) and Rudnick and Gao (2003), respectively. Data for Hawaiian OIB are from Feigenson et al. (1996). (b) Ti/Y versus Ti/Zr diagram (after Hergt et al. (1991)). The fields for MORB, granite and sediment based on the Post-Archean Terrestrial Shale are from Taylor and McLennan (1995).

Therefore, these Early Carboniferous basaltic rocks and dacites in the western Luliang Uplift were formed in an island arc setting and were derived from a mantle wedge contaminated by subducted fluid (Kay, 1984; Münker et al., 2004) and juvenile lower crust, which is also confirmed by the La/Nb-La and Nb/Th-Nb tectonic discrimination diagram (Fig. 12c, d). Also, the basalts have high TiO_2 contents and show the geochemical signature of within-plate basalts except for their resemblance to MORB (Fig. 12e, f). The basaltic and rhyodacite volcanic rock association from the wells (M201, MD2 and MD4) in the northern part of Xiayan High resembles bimodal feature, reflecting a potential extensional tectonic setting, which is in good agreement with development of homochronous graben basin in the western Luliang Uplift. Therefore, we suggest that an emerging intra-arc or back-arc rift existed in the western Luliang Uplift during the Early Carboniferous.

The Early Carboniferous volcanic rocks are heterogeneously distributed in the Xiayan High and exhibit contrasting geochemical features. The petrological and geochemical features and their spatio-temporal variations are not only the key factors to evaluate their tectonic settings (Condie, 1988; Barbarin, 1999), but also widely used to identify subduction polarity (Lopez-Escobar et al., 1979; Winter, 2001; Eyuboglu et al., 2011). In general, low-K tholeiitic magmas are considered to form close to the trench and high-K magmas (shoshonitic) are generated progressively from the trench in subduction settings. It has been clearly

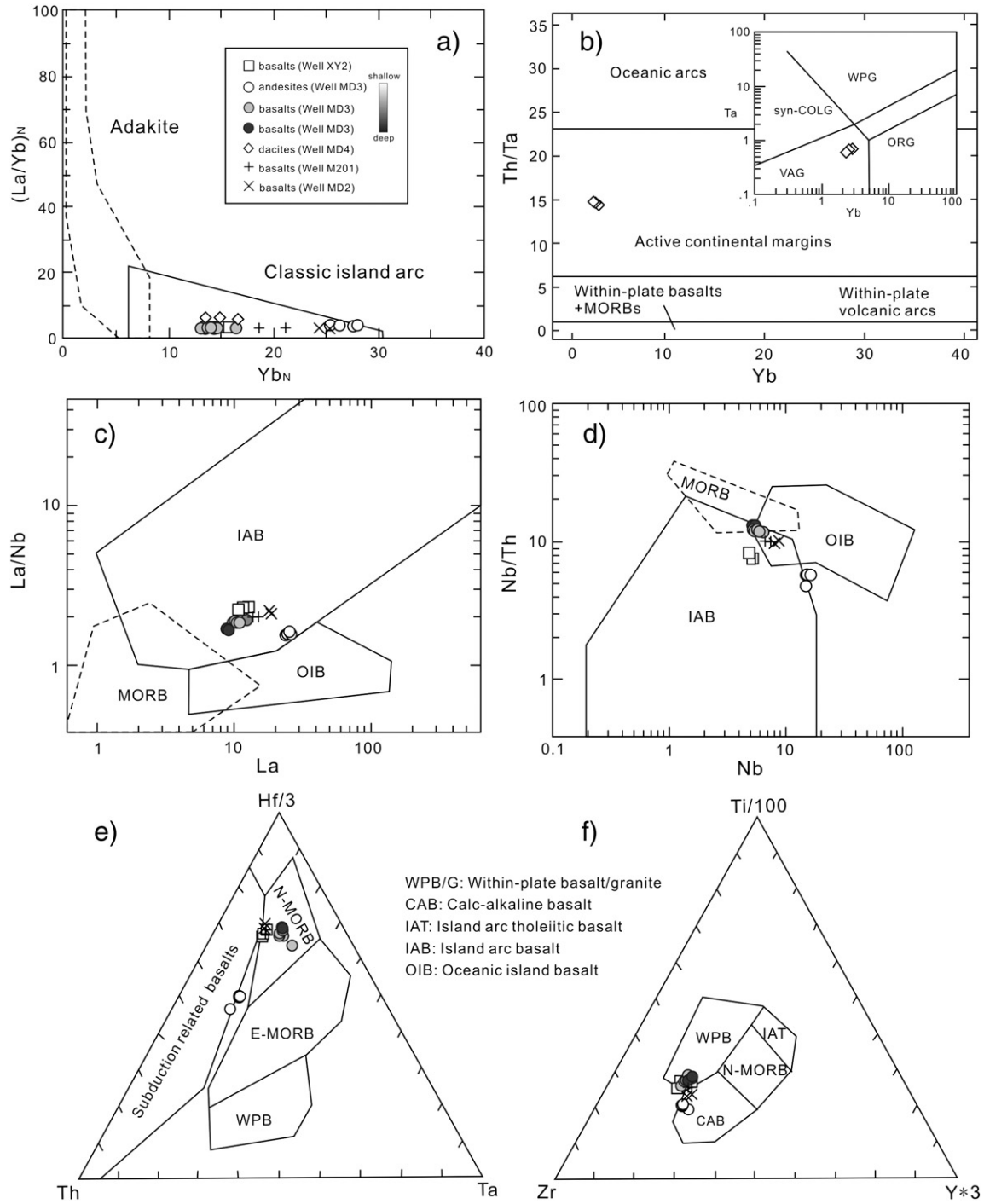


Fig. 12. Tectonic discrimination diagram with trace element plots of the Early Carboniferous volcanic rocks in the western Luliang Uplift. (a) $(\text{La}/\text{Yb})_N$ versus Yb_N diagram (after Defant and Drummond (1990)). (b) Th/Ta versus Yb (after Gorton and Schandl (2000)) and Ta versus Yb diagrams for the dacites. WPG—within-plate granitoid; VAG—volcanic arc granitoid; Syn-COLG—syn-collision granitoid; ORG—ocean ridge granitoid. (c) La/Nb versus La and (d) Nb/Th versus Nb diagrams. (e) $\text{Hf}/3$ - Th - Ta diagram (after Wood et al. (1981)). (f) $\text{Ti}/100$ - Zr - $\text{Y}^{\star}3$ diagram (after Pearce and Cann (1973)). IAT—Island arc tholeiitic; WPB—within-plate basalt; CAB—Calc-alkaline basalt.

demonstrated that the western Luliang Uplift represents an Early Carboniferous island arc based on the above discussion. The Early Carboniferous magmatism in the western Luliang Uplift started along the southern margin of the arc with low-K tholeiitic basalt from well XY2 (Fig. 6c). The intensity of this magmatism decreased toward the north, and shows a northward transition to calc-alkaline magmatism at the position of well MD3 (Fig. 6c). Further north, the magmatic activity intensified along the northern margin of Xiayan High (i.e., the position of wells MD2, MD4 and M201), with a transition into high-K calc-alkaline volcanism with bimodal characteristics. Such spatial and

temporal variations of Early Carboniferous arc magmatism from tholeiitic to calc-alkaline series in the south to high-K calc-alkaline to shoshonitic affinities in the north in the Xiayan High clearly suggest Early Carboniferous northward subduction (Fig. 13).

The western Luliang Uplift shows the tectonic pattern of high-sag-high from south to north during the Early Carboniferous. However, the Xiayan High in the south of western Luliang Uplift shows different sedimentary filling from that in the Yingxi Sag. The Xiayan High sedimentary assemblages include diatomaceous siltstone and mudstone interbedded with undeformed tholeiitic to calc-alkaline basaltic rocks and

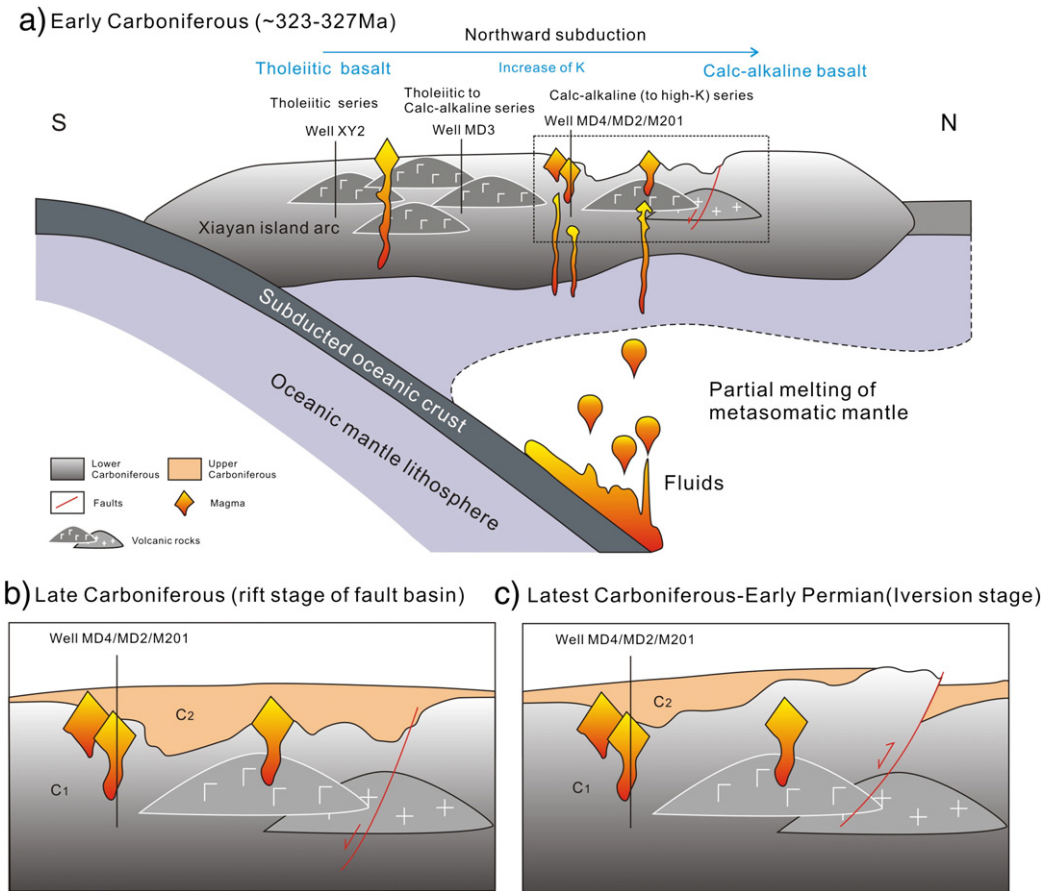


Fig. 13. Schematic diagram showing the geodynamic setting and basin evolution in the western Luliang Uplift. (a) Northward subduction basin system results in the formation of the Early Carboniferous island arc basin system; (b) intra-arc syn-rift basin evolution stage in the Late Carboniferous; and (c) basin inversion stage during the latest Carboniferous to Early Permian.

tuff, as well as minor limestone, which are typical sedimentary features of oceanic forearc basin (Scholl and Creager, 1973; Stewart, 1978). In addition, the Early Carboniferous strata show superimposition of multiple volcanic domal seismic reflection feature and sedimentary sequence with heterogeneous thickness, suggesting a sedimentary formation of syn-growth arc. Furthermore, the Yingxi Sag is dominated by Early Carboniferous bimodal volcanic rocks and proximal sandy conglomerate which accumulated in the arc-related extensional basin, and possibly represents a contemporaneous intra-arc basin. Therefore, we infer that northward subduction of Junggar Ocean occurred in the western Luliang Uplift during the Early Carboniferous, and gave rise to an island arc basin system with the development of forearc and intra-arc basins.

6.2. Tectonic link with the West Junggar terrane and its implication

Previous geochemical and geophysical data demonstrate that the Karamaili suture zone in the East Junggar terrane possibly extended to the Darbut suture zone in the southern West Junggar terrane via the Luliang Uplift of Junggar Basin (Kuang, 1993; Zhai et al., 2002; Chen et al., 2013; Li et al., 2014). The East and West Junggar terranes are composed of arc and accretionary complexes and preserve critical evidence for Late Devonian to Early Carboniferous intra-oceanic subduction and terrane amalgamation (Xiao et al., 2008; Long et al., 2010; Geng et al., 2011; Zhang et al., 2011b; Long et al., 2012; Tang et al., 2012). The recent recognition of a Carboniferous island arc in the eastern Luliang Uplift provides robust evidence for the westward extension of the East Junggar ancient subduction zone (Li et al., 2014, 2015-b). The distribution of Carboniferous magmatic units and their tectonostratigraphic evolution suggest that the East Junggar terrane (i.e., Karamaili area) and eastern Luliang Uplift share a similar tectonic evolution history. In

this study, we propose that there was a northward subduction system in the western Luliang Uplift in the Early Carboniferous, further attesting to the existence of Early Carboniferous Luliang arc. Most of the previous investigations were concentrated on the West Junggar terrane, lack of systematic data for the comparison between the western Luliang Uplift and West Junggar terrane.

The southern West Junggar terrane matches with the western Luliang Uplift, exhibiting common tectonic features. In the southern West Junggar terrane, the Carboniferous strata exposed in the southern West Junggar terrane (Darbut area) consist mainly of basalt, andesite, dacite, rhyolite and tuff from the Tailegula, Baogutu and Xibeikulasi Formations, with zircon U-Pb ages ranging from 328 to 357.5 Ma (Wang and Zhu, 2007; Guo et al., 2010; Yin et al., 2010; Geng et al., 2011). These rocks show consistently depleted Sr-Nd isotopic compositions and enrichment of LILEs and depletion of HFSEs (e.g., Nb and Ta), and are interpreted as products of a northwestward intra-oceanic subduction system of Junggar ocean during the Early Carboniferous (Tang et al., 2010; Geng et al., 2011; Zhang et al., 2011b). Meanwhile, a coeval Early Carboniferous back-arc basin likely developed in the Darbut area as inferred from the geochemical and geochronological analysis of the Darbut ophiolitic complex (G.X. Yang et al., 2012). The presence of Permian A-type granites and molasses in the West Junggar terrane implies a Late Carboniferous to Permian tectonic transition from subduction to closure of oceanic basin (Han et al., 2006; Zhou et al., 2008; Chen et al., 2010), and also indicates a denudation of crustal materials during this period (Li et al., 2015-a,b). Late Carboniferous intrusions and minor residual volcanic rocks show geochemical characteristics comparable with typical adakite and high-Mg andesite, suggesting that a ridge subduction might have occurred in the Darbut area at that time (Geng et al., 2009; Liu et al., 2009; Tang et al., 2010; Yin

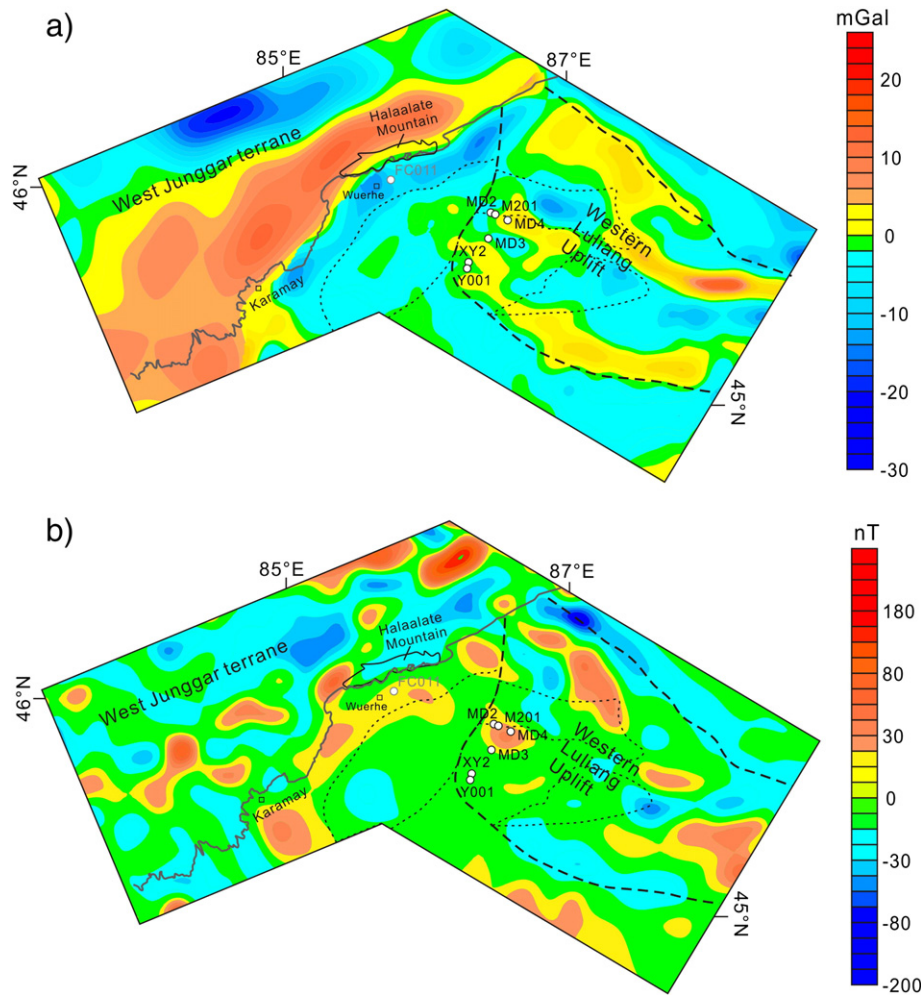


Fig. 14. Layer stripping residual gravity (a) and magnetic (b) anomaly maps in 1:200,000 scale for the western Luliang Uplift and adjacent West Junggar terrane.

et al., 2010; Ma et al., 2012; Tang et al., 2012). Our study shows that the western Luliang Uplift is dominated by a northward subduction with an initial arc-related rift basin during the Early Carboniferous, which facilitated the input of slab fluids into the mantle wedge to generate a subduction-related tholeiitic to calc-alkaline lavas (Fig. 12). The long stratigraphic hiatus caused a large unconformity between the Lower Carboniferous to Middle Permian strata (Fig. 2). Several geological similarities also exist between the western Luliang Uplift and southern West Junggar terrane. Fig. 14 shows the layer stripping residual gravity and magnetic signatures. Both of the two arc massifs are bounded by steep gravity gradient belts and show high gravity anomalies (Fig. 14a). Comparably, the southern West Junggar exhibits relative higher positive gravity anomalies (up to 12 mGal) than those in the western Luliang Uplift, suggesting the occurrence of more high-density volcanic rocks (Fig. 14a). The western Luliang Uplift and southern West Junggar terrane show similar magnetic anomaly features with multiple small positive anomaly within an overall insignificant or negative magnetic anomaly (Fig. 14b), indicating a unified geological feature. Therefore, the analogous tectonostratigraphic units and common structure in planar view suggest that the western Luliang Uplift and southern West Junggar terrane experienced a common tectonic evolution in the Early Carboniferous and may represent parts of the same tectonic zone.

Nevertheless, there are some significant differences between these two terranes. The southern West Junggar terrane is characterized by NE-trending major faults and fault-bounded Darbut arc massifs and accretionary complexes, unlike the NW-oriented faults of the western

Luliang Uplift as represented by gravity gradient belt (Fig. 14a). Recent paleomagnetic data suggest that this difference probably results from large-scale rotations of the West Junggar terrane relative to the present Junggar Basin during the Late Carboniferous (Yi et al., 2015). In addition, a relatively complete record of Lower Permian strata (P_{1j} —Jiamuhe Formation and P_{1f} —Fengcheng Formation) was preserved in the piedmont sag (Mahu Sag) of the West Junggar terrane, and becomes progressively thick toward the West Junggar terrane, with an eastward migration of the basin depocenter (Fig. 15), supporting the interpretation that the West Junggar ocean was shrinking and closed during this period (Li et al., 2015-a,b; Yi et al., 2015). The onlapped phenomenon of Lower Permian strata toward the Xiayan High potentially suggests that an earlier uplift occurred in the western Luliang Uplift, indicating that the Luliang arc had been accreted into the Wulungu terrane in the Early Permian. The widespread large unconformities between the terrigenous Middle Permian strata and the underlying units may define the upper time limit of oceanic closure in the western Luliang Uplift and West Junggar terrane as Middle Permian.

Based on the above discussion, a schematic model of evolution of the northern Junggar Basin and adjacent regions during the Late Paleozoic is illustrated in Fig. 16. In the Early Carboniferous, the Junggar Ocean existed in the Junggar region. A northward subduction stretching across the northern Junggar region occurred as represented by the Karamaili and Darbut ophiolite, and formed the Yemaquan composite arc, Luliang arc and Darbut arc, accompanied by the development of a back-arc basin (Li, 2004; Zhang et al., 2011b; G.X. Yang et al., 2012) and an initial intra-arc basin (this study). In addition, another northward subduction

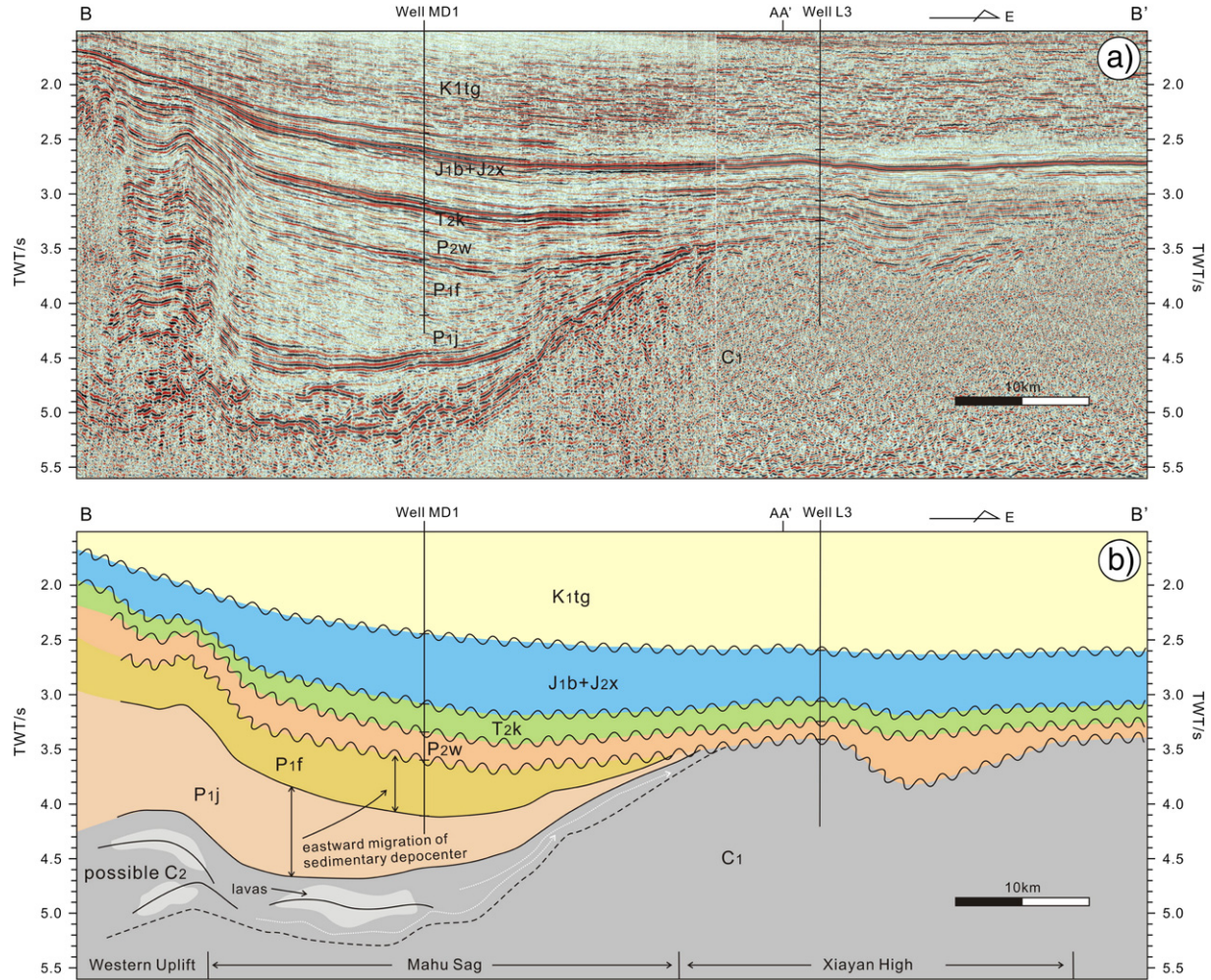


Fig. 15. Re-interpreted seismic profile BB' and geological interpretation at the junction between the western Luliang Uplift and adjacent West Junggar terrane in relation to their tectonic links. See text for discussion. K₁tg—Lower Cretaceous Tugulu Group; J₁b—Lower Jurassic Badaowan Formation; J₂x—Middle Jurassic Xishanyao Formation; T₂k—Middle Triassic Karamay Formation; P₂w—Middle Permian Wuerhe Formation; P₁f—Lower Permian Fengcheng Formation; P₁j—Lower Permian Jiamuhe Formation; C₂—Upper Carboniferous system; and C₁—Lower Carboniferous system.

potentially took place in the Wulungu area (Fig. 16a). During the Late Carboniferous, the oceanic basin of the East Junggar terrane was closed as inferred on the basis of the available geochronological data and paleontological information (Shu and Wang, 2003). Continuing subduction in the Junggar basin resulted in further development of intra-arc basin in the Luliang arc and back-arc basin of West Junggar as well as the amalgamation of the Luliang arc and Wulungu terrane. Importantly, a counterclockwise rotation of West Junggar terrane relative to Junggar Basin caused the bending of the Darbut arc during this period (Fig. 16b). In the Early Permian, several island arcs and accretionary prisms (including the Darbut ophiolite) were accreted into the previously formed accretionary complexes of West Junggar terrane. In combination with the large-scale uplift of the Luliang arc and Darbut arc, it is clear that the north Junggar Basin and East and West Junggar terrane culminated the amalgamation (Fig. 16c). The whole Junggar terrane was characterized by northward/northwestward intra-oceanic subduction and southward/southeastward accretion process during the Paleozoic (e.g., Xiao et al., 2008; Tang et al., 2010; Geng et al., 2011; Long et al., 2012; G.X. Yang et al., 2012; this study), indicating that the Junggar Ocean might have finally disappeared in the southern Junggar basin in the form of consumption or remnant. These results provide further support for a collaged Junggar basement of Paleozoic arcs, accretionary complexes and trapped oceanic crust (Zheng et al., 2007; Xiao et al., 2008; Xiao and Santosh, 2014).

7. Conclusions

The western Luliang Uplift is dominated by the Early Carboniferous tholeiitic to calc-alkaline basalt, basaltic andesite and dacite interbedded with multiple sets of thin siltstone. The petrographic and geochemical data suggest that the basaltic rocks were derived from depleted mantle modified by slab-derived fluids in an island arc environment, whereas the dacites with I-type granite affinity formed from a juvenile lower crustal source. These coeval volcanic rocks show a temporal variation of tholeiitic to calc-alkaline series in the south to calc-alkaline to shoshonitic series in the north, clearly indicating a northward subduction. The extensional structural deformation and basin fill pattern suggest that the western Luliang Uplift represented an island arc basin system with the development of forearc and intra-arc basins in the Early Carboniferous.

The western Luliang Uplift and southern West Junggar terrane exhibit similar tectonostratigraphic evolution and plan view structure, suggesting that they experienced a common tectonic evolution from Carboniferous subduction-accretion process to Early Permian amalgamation in the Late Paleozoic. Their coupling relationship also confirms the Luliang Uplift as a link with the East and West Junggar terranes, providing important constraints on the Late Paleozoic tectonic paleogeography and basement architecture of the Junggar terrane.

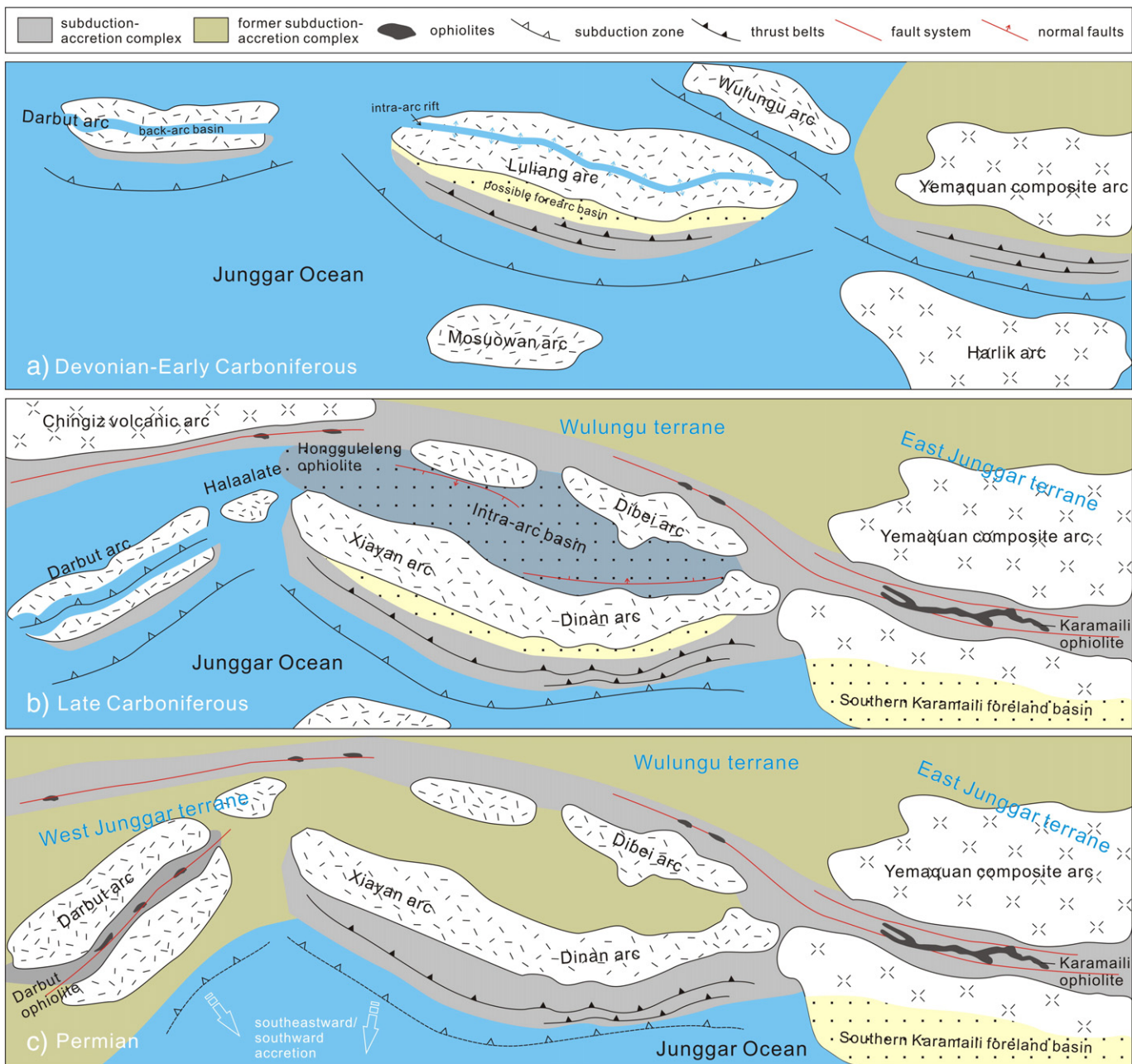


Fig. 16. Cartoons illustrating the reconstruction of the Luliang Uplift and adjacent East and West Junggar terranes during the Paleozoic (data compiled from Geng et al. (2009); Tang et al. (2010); Geng et al. (2011); Zhang et al. (2011a,b); Tang et al. (2012); G.X. Yang et al. (2012); Li et al. (2015-a); and Yi et al. (2015)).

Acknowledgments

The Xinjiang Oilfield Company kindly supplied gravity and magnetic data, seismic profiles and borehole core samples in the western Luliang Uplift. Dr. Timothy Horscroft from Elsevier is acknowledged for his invitation to submit this manuscript. We are very grateful to the Associate Editor Prof. Wenjiao Xiao and two anonymous reviewers, whose polishing work and generous comments have greatly improved the manuscript. We also express our appreciation to Drs. Qili Li, Chaofeng Li and Mengning Dai for their laboratory assistance. This research was financially supported by the National Science and Technology Major Project (2011ZX05008-001, 2011ZX05002-002), the National Natural Science Foundation of China (41272237, 40739906), and the Chinese State 973 Project (2011CB201100). This work contributes to the 1000 Talents Award to M. Santosh from the Chinese Government, and is also a contribution to IGCP592.

References

- Bally, A.W., 1983. Seismic expression of structural styles: a picture and work atlas. American Association of Petroleum Geologists Studies in Geology Series 15.
- Barbarin, B., 1999. A review of the relationships between granitoid types, their origins and their geodynamic environments. *Lithos* 46, 605–626.
- Bian, W., Hornung, J., Liu, Z., Wang, P., Hinderer, M., 2010. Sedimentary and palaeoenvironmental evolution of the Junggar Basin, Xinjiang, Northwest China. *Palaeobiology and Palaeoenvironment* 90, 175–186.
- Buslov, M.M., Saphonova, I.Yu., Watanabe, T., Obut, O.T., Fujiwara, Y., Iwata, K., Semakov, N.N., Sugai, Y., Smirnova, L.V., Kazansky, A.Yu., 2001. Evolution of the Paleo-Asian Ocean (Altai-Sayan Region, Central Asia) and collision of possible Gondwana derived terranes with the southern marginal part of the Siberian continent. *Geoscience Journal* 5, 203–224.
- Carroll, A.R., Liang, Y., Graham, S.A., Xiao, X., Hendrix, M.S., Chu, J., McKnight, C.L., 1990. Junggar Basin, northwest China: trapped Late Paleozoic ocean. *Tectonophysics* 181, 1–14.
- Chen, B., Jahn, B.M., 2004. Genesis of post-collisional granitoids and basement nature of the Junggar Terrane, NW China: Nd-Sr isotope and trace element evidence. *Journal of Asian Earth Sciences* 23, 691–703.

- Chen, F., Siebel, W., Satir, M., Terzioglu, N., Saka, K., 2002. Geochronology of the Karadere basement (NW Turkey) and implications for the geological evolution of the Istanbul zone. *International Journal of Earth Sciences* 91, 469–481.
- Chen, J.F., Han, B.F., Ji, J.Q., Zhang, L., Xu, Z., He, G.Q., Wang, T., 2010. Zircon U-Pb ages and tectonic implications of Paleozoic plutons in northern West Junggar, North Xinjiang, China. *Lithos* 115, 137–152.
- Chen, S., Guo, Z.J., Pe-Piper, G., Zhu, B.B., 2013. Late Paleozoic peperites in West Junggar, China, and how they constrain regional tectonic and palaeoenvironmental setting. *Gondwana Research* 23, 666–681.
- Clift, P.D., Degnan, P.J., Hannigan, R., Blusztajn, J., 2000. Sedimentary and geochemical evolution of the Dras forearc basin, Indus suture, Ladakh Himalaya, India. *Geological Society of America Bulletin* 112, 450–466.
- Coleman, R., 1989. Continental growth of Northwest China. *Tectonics* 8, 621–635.
- Condie, K.C., 1988. Precambrian tectonic settings and secular geochemical variations. *International Symposium on Geochemistry and Mineralization of Proterozoic Mobile Belt (abstracts)*, pp. 14–15.
- Cullen, J.T., Field, M.P., Sherrell, R.M., 2001. Determination of trace elements in filtered suspended marine particulate material by sector field HR-ICP-MS. *Journal of Analytical Atomic Spectrometry* 16, 1307–1312.
- Defant, M.J., Drummond, M.S., 1990. Derivation of some modern arc magmas by melting of young subduction lithosphere. *Nature* 347, 662–665.
- Draut, A.E., Clift, P.D., 2006. Sedimentary processes in modern and ancient oceanic arc settings: evidence from the Jurassic Talkeetna Formation of Alaska and the Mariana and Tonga arcs, western Pacific. *Journal of Sedimentary Research* 76, 493–514.
- Eyboglu, Y., Santos, M., Bektas, O., Ayhan, S., 2011. Arc magmatism as a window to plate kinematics and subduction polarity: example from the eastern Pontides belt, NE Turkey. *Geoscience Frontiers* 2, 49–56.
- Feigenson, M.D., Patino, L.C., Carr, M.J., 1996. Constraints on partial melting imposed by rare earth element variations in Mauna Kea basalts. *Journal of Geophysical Research* 101, 11815–11829.
- Frey, F.A., Weis, D., Borisova, A.Y.U., Xu, G., 2002. Involvement of continental crust in the formation of the Cretaceous Kerguelen Plateau: new perspectives from ODP Leg 120 sites. *Journal of Petrology* 43, 1207–1239.
- Geng, H.Y., Sun, M., Yuan, C., Xiao, W.J., Xian, W.S., Zhao, G.C., Zhang, L.F., Wong, K., Wu, F.Y., 2009. Geochemical, Sr–Nd and zircon U-Pb–Hf isotopic studies of Late Carboniferous magmatism in the West Junggar, Xinjiang: implications for ridge subduction? *Chemical Geology* 266, 364–389.
- Geng, H.Y., Sun, M., Yuan, C., Zhao, G.C., Xiao, W.J., 2011. Geochemical and geochronological study of early Carboniferous volcanic rocks from the West Junggar: petrogenesis and tectonic implications. *Journal of Asian Earth Sciences* 42, 854–866.
- Goolaerts, A., Mattielli, N., de Jong, J., Weis, D., Scotes, J.S., 2004. Hf and Lu isotopic reference values for the zircon standard 91500 by MC-ICP-MS. *Chemical Geology* 206, 1–9.
- Gorton, M.P., Schandl, E.V., 2000. From continents to island arcs: a geochemical index of tectonic setting for arc-related and within-plate felsic to intermediate volcanic rocks. *The Canadian Mineralogist* 38, 1065–1073.
- Guo, L.S., Liu, Y.L., Wang, Z.H., Song, D., Xu, J.F., Su, L., 2010. The zircon U-Pb LA-ICPMS geochronology of volcanic rocks in Baogutu areas, western Junggar. *Acta Petrologica Sinica* 26, 471–477 (in Chinese with English abstract).
- Han, B.F., Ji, J.Q., Song, B., Chen, L.H., Zhang, L., 2006. Late Paleozoic vertical growth of continental crust around the Junggar Basin, Xinjiang, China (part I): timing of postcollisional plutonism. *Acta Petrologica Sinica* 22, 1077–1086 (in Chinese with English abstract).
- Hart, S.R., 1988. Heterogeneous mantle domains: signature, genesis and mixing chronologies. *Earth and Planetary Science Letters* 90, 273–296.
- Hartmann, L.A., Santos, J.O.S., 2004. Predominance of high Th/U magmatic zircons in Brazilian shield sandstones. *Geology* 32, 73–76.
- Hastie, A.R., Kerr, A.C., Pearce, J.A., Mitchell, S.F., 2007. Classification of altered volcanic island arc rocks using immobile trace elements: development of the Th-Co discrimination diagram. *Journal of Petrology* 48, 2341–2357.
- Hawkins, J.W., 2003. Geology of supra-subduction zones: implications for the origin of ophiolites. In: Dilek, Y., Newcomb, S. (Eds.), *Ophiolite concept and the evolution of geological thought*. Geological Society of America Special Paper 373, pp. 227–268.
- He, D.F., Li, D., Fan, C., Yang, X.F., 2013. Geochronology, geochemistry and tectonostratigraphy of Carboniferous strata of the deepest Well Moshen-1 in the Junggar Basin, Northwest China: insights into the continental growth of Central Asia. *Gondwana Research* 24, 560–577.
- Hergt, J.M., Peate, D.W., Hawkesworth, C.J., 1991. The petrogenesis of Mesozoic Gondwana low-Ti flood basalts. *Earth and Planetary Science Letters* 105, 134–148.
- Hu, A.Q., Jahn, B.M., Zhang, G.X., Chen, Y.B., Zhang, Q.F., 2000. Crustal evolution and Phanerozoic crustal growth in northern Xinjiang: Nd isotopic evidence. Part I. Isotopic characterization of basement rocks. *Tectonophysics* 328, 15–51.
- Iizuka, T., Hirata, T., 2005. Improvements of precision and accuracy in in-situ Hf isotope microanalysis of zircon using the laser ablation-MC-ICPMS technique. *Chemical Geology* 220, 121–137.
- Jahn, B.M., Condie, K.C., 1995. Evolution of the Kaapvaal-craton as viewed from geochemical and Sm–Nd isotopic analyses of intracratonic pelites. *Geochimica et Cosmochimica Acta* 59, 2239–2258.
- Jahn, B.M., Wu, F.Y., Chen, B., 2000. Massive granitoid generation in Central Asia: Nd isotope evidence and implication for continental growth in the Phanerozoic. *Episodes* 23, 82–92.
- Jahn, B.M., Natal'in, B.A., Windley, B.F., Dobretsov, N., 2004. Phanerozoic continental growth in Central Asia. *Journal of Asian Earth Sciences* 23, 599–603.
- Jian, P., Liu, D.Y., Zhang, Q., Zhang, F.Q., Shi, Y.R., Shi, G.H., Zhang, L.Q., Tao, H., 2003. SHRIMP dating of ophiolite and leucocratic rocks within ophiolite. *Earth Science Frontiers* 10, 439–455 (in Chinese with English abstract).
- Jian, P., Liu, D.Y., Shi, Y.R., Zhang, F.Q., 2005. SHRIMP dating of SSZ ophiolites from northern Xinjiang Province, China: implications for generation of oceanic crust in the central Asian orogenic belt. In: Sklyarov, E.V. (Ed.), *Structural and Tectonic Correlation Across the Central Asian Orogenic Collage: Northeastern Segment. Guidebook and Abstract Volume of the Siberian Workshop ICP-480*, p. 246.
- Johnson, K.T.M., Dick, H.J.B., Shimizu, N., 1990. Melting in the oceanic upper mantle: an ion microprobe study of diopside in abyssal peridotites. *Journal of Geophysical Research* 95, 2661–2678.
- Kay, R.W., 1984. Elemental abundances relevant for identification of magma sources. *Philosophical Transactions of the Royal Society of London A* 310, 535–547.
- Kovalenko, V.I., Yarmolyuk, V.V., Kovach, V.P., Kotov, A.B., Kozakov, I.K., Salnikova, E.B., Larin, A.M., 2004. Isotopic provinces, mechanism of generation and sources of the continental crust in the Central Asian mobile belt: geological and isotopic evidence. *Journal of Asian Earth Sciences* 23, 605–627.
- Kröner, A., Hegner, E., Lehmann, B., Heinhorst, J., Wingate, M.T.D., Liu, D.Y., Ermelov, P., 2008. Palaeozoic arc magmatism in the Central Asian Orogenic Belt of Kazakhstan: SHRIMP zircon ages and whole-rock Nd isotopic systematics. *Journal of Asian Earth Sciences* 32, 118–130.
- Kröner, A., Alexeev, D.V., Rojas-Agramonte, Y., Hegner, E., Wong, J., Xia, X., Belousova, E., Mikolaichuk, A.V., Seltmann, R., Liu, D., Kiselev, V.V., 2013. Mesoproterozoic (Grenville) terranes in the Kyrgyz North Tianshan: Zircon ages and Nd–Hf isotopic constraints on the origin and evolution of basement blocks in the southern Central Asian Orogen. *Gondwana Research* 23, 272–295.
- Kröner, A., Kovach, V., Belousova, E., Hegner, E., Dolgopolova, A., Seltmann, R., Alexeev, D.V., Hoffmann, J.E., Wong, J., Sun, M., Cai, K., Wang, T., Tong, Y., Wilde, S.A., Degtaryev, K.E., Rytsev, E., 2014. Reassessment of continental growth during the accretionary history of the Central Asian Orogenic Belt. *Gondwana Research* 25, 103–125.
- Kuang, J., 1993. Terrane connection, formation and evolution of Junggar Basin. *Xinjiang Petroleum Geology* 14, 126–132 (in Chinese with English abstract).
- Leeder, M.R., 2011. Tectonic sedimentology: sediment systems deciphering global to local tectonics. *Sedimentology* 58, 2–56.
- Li, J.Y., 2004. Late Neoproterozoic and Paleozoic tectonic framework and evolution of eastern Xinjiang NW China. *Geological Review* 50, 304–322 (in Chinese with English abstract).
- Li, X.H., Liu, Y., Li, Q.L., Guo, C.H., Chamberlain, K.R., 2009. Precise determination of Phanerozoic zircon Pb/Pb age by multi-collector SIMS without external standardization. *Geochemistry, Geophysics, Geosystems* 10. <http://dx.doi.org/10.1029/2009GC002400>
- Li, X.H., Li, W.X., Wang, X.C., Li, Q.L., Liu, Y., Tang, G.Q., Gao, Y.Y., Wu, F.Y., 2010. SIMS U-Pb zircon geochronology of porphyry Cu–Au–(Mo) deposits in the Yangtze River Metallogenetic Belt, eastern China: magmatic response to early Cretaceous lithospheric extension. *Lithos* 119, 427–438.
- Li, D., He, D.F., Santos, M., Tang, J.Y., 2014. Petrogenesis of Late Paleozoic volcanics from the Zhaheba depression, East Junggar: insights into collisional event in an accretionary orogen of Central Asia. *Lithos* 184–187, 167–193.
- Li, D., He, D.F., Qi, X.F., Zhang, N.N., 2015a. How was the Carboniferous Balkhash–West Junggar remnant ocean filled and closed? Insights from the Well Tacan-1 strata in the Tacheng Basin, NW China. *Gondwana Research* 27, 342–362.
- Li, D., He, D.F., Santos, M., Ma, D.L., Tang, J.Y., 2015b. Tectonic framework of the northern Junggar Basin part I: the eastern Luliang Uplift and its link with the East Junggar terrane. *Gondwana Research* 27, 1089–1109.
- Liu, X.J., Xu, J.F., Wang, S.Q., Hou, Q.Y., Bai, Z.H., Lei, M., 2009. Geochemistry and dating of E-MORB type mafic rocks from Dalabute ophiolite in West Junggar, Xinjiang and geological implications. *Acta Petrologica Sinica* 25, 1373–1389.
- Long, X.P., Yuan, C., Sun, M., Xiao, W.J., Zhao, G.C., Wang, Y.J., Cai, K.D., Xia, X.P., Xie, L.W., 2010. Detrital zircon U-Pb ages and Hf isotopes of the early Paleozoic flysch sequence in the Chinese Altai, NW China: new constraints on depositional age, provenance and tectonic evolution. *Tectonophysics* 480, 213–231.
- Long, X.P., Yuan, C., Sun, M., Safonova, I., Xiao, W.J., Wang, Y.J., 2012. Geochemistry and U-Pb detrital zircon dating of Paleozoic graywackes in East Junggar, NW China: insights into subduction-accretion processes in the southern Central Asian Orogenic Belt. *Gondwana Research* 21, 637–655.
- Lopez-Escobar, L.M., Frey, F.A., Jorge, O., 1979. Geochemical characteristics of central Chile (33° – 34° S) granitoids. *Contribution to Mineralogy and Petrology* 70, 439–450.
- Ludwig, K.R., 2001. *Users Manual for Isoplots/Ex rev. 2.49*. Berkeley Geochronology Centre Special Publication No. 1a, (56 pp.).
- Ma, C., Xiao, W.J., Windley, B.F., Zhao, G.P., Han, C.M., Zhang, J.E., Luo, J., Li, C., 2012. Tracing a subducted ridge-transform system in a late Carboniferous accretionary prism of the southern Altaids: orthogonal sanukitoid dyke swarms in western Junggar, NW China. *Lithos* 140–141, 152–165.
- Maniar, P.D., Piccoli, P.M., 1989. Tectonic discrimination of granitoids. *Geological Society of America Bulletin* 101, 635–643.
- McCann, T., Saintot, A., 2003. Tracing tectonic deformation using the sedimentary record. *Geological Society Special Publication* 208, 356.
- McDonough, W.F., 1990. Constraints on the composition of the continental lithospheric mantle. *Earth and Planetary Science Letters* 101, 1–18.
- Münker, C., Wörner, G., Yogodzinski, G., Churikova, T., 2004. Behaviour of high field strength elements in subduction zones: constraints from Kamchatka–Aleutian arc lavas. *Earth and Planetary Science Letters* 224, 275–293.
- Pearce, J.A., 1983. Role of the subcontinental lithosphere in magma genesis at active continental margins. In: Hawkesworth, C.J., Norry, M.J. (Eds.), *Continental Basalts and Mantle Xenoliths*. Shiva Publishing, Nantwich, pp. 230–249.
- Pearce, J.A., Cann, J., 1973. Tectonic setting of basic volcanic rocks determined using trace element analyses. *Earth and Planetary Science Letters* 19, 290–300.
- Plank, T., 2005. Constraints from Thorium/Lanthanum on sediment recycling at subduction zones and the evolution of the continents. *Journal of Petrology* 46, 921–944.

- Rojas-Agramonte, Y., Kröner, A., Demoux, A., Xia, X., Wang, W., Donskaya, T., Liu, D., Sun, M., 2011. Detrital and xenocrystic zircon ages from the Neoproterozoic to Paleozoic arc terranes of Mongolia: significance for the origin of crustal fragments in the Central Asian Orogenic Belt. *Gondwana Research* 19, 751–763.
- Rollinson, H., 1993. *Using Geochemical Data: Evolution, Presentation, Interpretation*. Longman Scientific & Technical, UK, (344 pp.).
- Rudnick, R.L., Gao, S., 2003. Composition of the continental crust. In: Rudnick, R.L. (Ed.), *The Crust vol. 3*. Elsevier, pp. 1–64.
- Safonova, I.V., Utsunomiya, A., Kojima, S., Nakae, S., Tomurtogoo, O., Filippov, A.N., Koizumi, K., 2009. Pacific superplume-related oceanic basalts hosted by accretionary complexes of Central Asia, Russian Far East and Japan. *Gondwana Research* 16, 587–608.
- Safonova, I., Seltmann, R., Kröner, A., Gladkochub, D., Schulmann, K., Xiao, W., Kim, J., Komiya, T., Sun, M., 2011. A new concept of continental construction in the Central Asian Orogenic Belt (compared to actualistic examples from the Western Pacific). *Episodes* 34, 186–196.
- Scholl, D.W., Creager, J.S., 1973. Geologic synthesis of leg 19 (DSDP) results: far north Pacific, Aleutian Ridge, and Bering Sea. In: Creager, J.S., Scholl, D.W. (Eds.), *Initial Reports of the Deep Sea Drilling Project 19*. U.S. Government Printing Office, Washington, D.C., pp. 897–913.
- Seltmann, R., Porter, T.M., 2005. The porphyry Cu–Au/Mo deposits of central Eurasia I. Tectonic, geologic and metallogenic setting, and significant deposits. In: Porter, T.M. (Ed.), *Super Porphyry Copper and Gold Deposits: A Global Perspective* vol. 2. PGC Publishing, Adelaide, pp. 467–512.
- Sen, C., Dunn, T., 1994. Dehydration melting of a basaltic composition amphibolite at 1.5 and 2.0 GPa: implications for the origin of adakites. *Contributions to Mineralogy and Petrology* 117, 394–409.
- Şengör, A.M.C., Natal'in, B.A., Burtman, U.S., 1993. Evolution of the Altai tectonic collage and Paleozoic crustal growth in Eurasia. *Nature* 364, 209–304.
- Shen, P., Shen, Y.C., Liu, T.B., Meng, L., Dai, H.W., Yang, Y.H., 2009. Geochemical signature of porphyries in the Baogutu porphyry copper belt, western Junggar, NW China. *Gondwana Research* 16, 227–242.
- Shen, P., Shen, Y.C., Wang, J.B., Zhu, H.P., Wang, L.J., Meng, L., 2010. Methane-rich fluid evolution of the Baogutu porphyry Cu–Mo–Au deposit, Xinjiang, NW China. *Chemical Geology* 275, 78–98.
- Shu, L.S., Wang, Y.J., 2003. Late Devonian-Early Carboniferous radiolarian fossils from siliceous rocks of the Calomel ophiolite, Xinjiang. *Geological Review* 49, 408–412 (in Chinese with English abstract).
- Stacey, J.S., Kramers, J.D., 1975. Approximation of terrestrial lead isotope evolution by a two-stage model. *Earth and Planetary Science Letters* 26, 207–221.
- Stewart, R.J., 1978. Neogene volcanoclastic sediments from Atka Basin, Aleutian Ridge. *American Association of Petroleum Geologists Bulletin* 62, 87–97.
- Su, Y.P., Tang, H.F., Hou, G.S., 2006. Geochemistry of aluminous A-type granites along Darabut tectonic belt in West Junggar, Xinjiang. *Geochimica* 35, 1–5 (in Chinese with English abstract).
- Su, Y., Zheng, J., Griffin, W.L., Tang, H., O'Reilly, S., Lin, X., 2010. Zircon U–Pb and Hf isotopes of volcanic rocks from the Batamayineishan formation in the eastern Junggar Basin. *Chinese Science Bulletin* 55, 4150–4161.
- Su, Y.P., Zheng, J.P., Griffin, W.L., Zhao, J.H., Tang, H.Y., Ma, Q., Lin, X.Y., 2012. Geochemistry and geochronology of Carboniferous volcanic rocks in the eastern Junggar terrane, NW China: implication for a tectonic transition. *Gondwana Research* 22, 1009–1029.
- Sun, S.S., McDonough, W.F., 1989. Chemical and isotopic systematics of ocean basalts: implication for mantle composition and processes. In: Saunders, A.D., Norry, M.J. (Eds.), *Magma in Ocean Basins*. Geological Society Special Publication 42, pp. 313–345.
- Tang, H.F., Su, Y.P., Liu, C.Q., Hou, G.S., Wan, Y.B., 2007. Zircon U–Pb age of the plagiogranite in Kalamaili belt, northern Xinjiang and its tectonic implications. *Geotectonica et Metallogenica* 31, 110–117 (in Chinese with English abstract).
- Tang, G.J., Wang, Q., Wyman, D.A., Li, Z.X., Zhao, Z.H., Jia, X.H., Jiang, Z.Q., 2010. Ridge subduction and crustal growth in the Central Asian Orogenic Belt: evidence from Late Carboniferous adakites and high-Mg diorites in the western Junggar region, northern Xinjiang (west China). *Chemical Geology* 227, 281–300.
- Tang, G.J., Wyman, D.A., Wang, Q., Li, J., Li, Z.X., Zhao, Z.H., Sun, W.D., 2012. Asthenosphere-lithosphere interaction triggered by a slab window during ridge subduction: trace element and Sr–Nd–Hf–Os isotopic evidence from Late Carboniferous tholeiites in the western Junggar area (NW China). *Earth and Planetary Science Letters* 329–330, 84–96.
- Taylor, S.R., McLennan, S., 1995. The geochemical composition of the continental crust. *Reviews of Geophysics* 33, 241–265.
- Ubatto, D., 2002. Zircon trace element geochemistry: partitioning with garnet and the link between U–Pb ages and metamorphism. *Chemical Geology* 184, 123–138.
- Wang, R., Zhu, Y.F., 2007. Geology of the Baobei Gold Deposit in western Junggar and zircon SHRIMP age of its wall-rocks, Western Junggar (Xinjiang, NW China). *Geological Journal of China Universities* 13, 590–602.
- Wang, F.Z., Yang, H.Z., Zheng, J.P., 2002. Geochemical characteristics and geological environment of basement volcanic rocks in Luliang, central region in Junggar Basin. *Acta Petrologica Sinica* 18, 9–16 (in Chinese with English abstract).
- Weimer, P., Davis, T.L., 1996. Applications of 3-D seismic data to exploration and production. *AAPG Studies in Geology No. 42 and SEG Geophysical Development Series No. 5*, p. 270.
- Wiedenbeck, M., Alle, P., Corfu, F., Griffin, W.L., Meier, M., Oberli, F., Vonquadt, A., Roddick, J.C., Speigel, W., 1995. Three natural zircon standards for U–Th–Pb, Lu–Hf, trace-element and REE analyses. *Geostandards Newsletter* 19, 1–23.
- Wilhem, C., Windley, B.F., Stampfli, G.M., 2012. The altaiids of Central Asia: a tectonic and evolutionary innovative review. *Earth-Science Reviews* 113, 303–341.
- Winchester, J.A., Floyd, P.A., 1977. Geochemical discrimination of different magmas series and their differentiation products using immobile elements. *Chemical Geology* 20, 325–343.
- Windley, B.F., Alexeiev, D.V., Xiao, W., Kröner, A., Badarch, G., 2007. Tectonic models for accretion of the Central Asian Orogenic Belt. *Journal of the Geological Society of London* 164, 31–47.
- Winter, J.D., 2001. *An Introduction to Igneous and Metamorphic Petrology*. New Jersey Prentice Hall, pp. 1–702.
- Wood, D.A., Marsh, N.G., Tarney, J., Joron, L.J., Fryer, P., Treuil, M., 1981. Geochemistry of igneous rocks recovered from a transect across the Mariana trough, arc, fore-arc, and trench, sites 453 through 461, Deep Sea Drilling Project Leg 60. In: Husson, D.M. (Ed.), *Initial Reports of the Deep Sea Drilling Project*, 60, pp. 611–645.
- Wu, X.Q., Liu, D.L., Wei, G.Q., Li, J., Li, Z.S., 2009. Geochemical characteristics and tectonic settings of Carboniferous volcanic rocks from Ludong–Wucaiwan area, Junggar Basin. *Acta Petrologica Sinica* 25, 55–66 (in Chinese with English abstract).
- Wu, F.Y., Yang, Y.H., Mitchell, R.H., Bellatreccia, F., Li, Q.L., Zhao, Z.F., 2010. In situ U–Pb and Nd–Hf–(Sr) isotopic investigations of zirconolite and calzirtite. *Chemical Geology* 277, 178–195.
- Xiao, W.J., Santosh, M., 2014. The western Central Asian Orogenic Belt: a window to accretionary orogenesis and continental growth. *Gondwana Research* 25, 1429–1444.
- Xiao, W.J., Windley, B.F., Yan, Q.R., Qin, K.Z., Chen, H.L., Yuan, C., Sun, M., Li, J.L., Sun, S., 2006. SHRIMP zircon age of the Aermantai ophiolite in the north Xinjiang area, China and its tectonic implications. *Acta Geologica Sinica* 80, 32–37 (in Chinese with English abstract).
- Xiao, W.J., Han, C.M., Yuan, C., Sun, M., Lin, S.F., Chen, H.L., Li, Z.L., Li, J.L., Sun, S., 2008. Middle Cambrian to Permian subduction-related accretionary orogenesis of North Xinjiang, NW China: implications for the tectonic evolution of Central Asia. *Journal of Asian Earth Sciences* 32, 102–117.
- Xiao, W.J., Windley, B.F., Kröner, A., 2009. Geodynamic evolution of Central Asia in the Paleozoic and Mesozoic. *International Journal of Earth Sciences* 98, 1185–1188.
- Xiao, W., Huang, B., Han, C., Li, J., 2010. A review of the western part of the Altaiids: a key to understanding the architecture of accretionary orogens. *Gondwana Research* 18, 253–273.
- Xiao, Y., Zhang, H., Shi, J.A., Su, B., Sakyi, P.A., Lu, X., Hu, Y., Zhang, Z., 2011. Late Paleozoic magmatic record of East Junggar, NW China and its significance: implication from zircon U–Pb dating and Hf isotope. *Gondwana Research* 20, 532–542.
- Xiao, W.J., Windley, B.F., Allen, M.F., Han, C.M., 2013. Paleozoic multiple accretionary and collisional tectonics of the Chinese Tianshan orogenic collage. *Gondwana Research* 23, 1316–1341.
- Xu, X., He, G.Q., Li, H.Q., Ding, T.F., Liu, X.Y., Mei, S.W., 2006. Basic characteristics of the Karamay ophiolitic mélange, Xinjiang, and its zircon SHRIMP dating. *Geology in China* 33, 470–475 (in Chinese with English abstract).
- Xu, Q.Q., Ji, J.Q., Zhao, L., Gong, J.F., Zhou, J., He, G.Q., Zhong, D.L., Wang, J.D., Griffiths, L., 2013a. Tectonic evolution and continental crust growth of Northern Xinjiang in northwestern China: remnant ocean model. *Earth-Science Reviews* 126, 178–205.
- Xu, X.W., Jiang, N., Li, X.H., Qu, X., Yang, Y.H., Mao, Q., Wu, Q., Zhang, Y., Dong, L.H., 2013b. Tectonic evolution of the East Junggar terrane: evidence from the Taheir tectonic window, Xinjiang, China. *Gondwana Research* 24, 578–600.
- Yakubchuk, A., 2004. Architecture and mineral deposit settings of the Altaiid orogenic collage: a revised model. *Journal of Asian Earth Sciences* 23, 761–779.
- Yang, J.H., Wu, F.Y., Wilde, S.A., Xie, L.W., Yang, Y.H., Liu, X.M., 2007. Tracing magma mixing in granite genesis: in situ U–Pb dating and Hf-isotope analysis of zircons. *Contributions to Mineralogy and Petrology* 153, 177–190.
- Yang, G.X., Li, Y.J., Wu, H.E., Zhong, X., Yang, B.K., Yan, C.X., Yan, J., Si, G.H., 2011. Geochronological and geochemical constrains on petrogenesis of the Huangyangshan A-type granite from the East Junggar, Xinjiang, NW China. *Journal of Asian Earth Sciences* 40, 722–736.
- Yang, G.X., Li, Y.J., Santosh, M., Gu, P.Y., Yang, B.K., Zhang, B., Wang, H.B., Zhang, X., Tong, L.L., 2012a. A Neoproterozoic seamount in the Paleoasian Ocean: evidence from zircon U–Pb geochronology and geochemistry of the Mayile ophiolitic mélange in West Junggar, NW China. *Lithos* 140–141, 53–65.
- Yang, G.X., Li, Y.J., Gu, P.Y., Yang, B.K., Tong, L.L., Zhang, H.W., 2012b. Geochronological and geochemical study of the Darbut Ophiolitic Complex in the West Junggar (NW China): implications for petrogenesis and tectonic evolution. *Gondwana Research* 21, 1037–1049.
- Yang, X.F., He, D.F., Wang, Q.C., Tang, Y., 2012c. Tectonostratigraphic evolution of the Carboniferous arc-related basin in the East Junggar Basin, northwest China: insights into its link with the subduction process. *Gondwana Research* 22, 1030–1046.
- Yi, Z.Y., Huang, B.C., Xiao, W.J., Yang, L.K., Qiao, Q.Q., 2015. Paleomagnetic study of Late Paleozoic rocks in the Tacheng Basin of West Junggar (NW China): implications for the tectonic evolution of the western Altaiids. *Gondwana Research* 27, 862–877.
- Yin, J.Y., Yuan, C., Sun, M., Long, X.P., Zhao, G.C., Wong, K.P., Geng, H.Y., Cai, K.D., 2010. Late Carboniferous high-Mg dioritic dikes in Western Junggar, NW China: geochemical features, petrogenesis and tectonic implications. *Gondwana Research* 17, 145–152.
- Zhai, G.M., Song, J.G., Jin, J.Q., Gao, W.L., 2002. *Plate Tectonic Evolution and its Relationship to Petroliferous Basins*. Petroleum Industry Press, Beijing, pp. 1–461 (in Chinese).
- Zhang, C., Huang, X., 1992. Age and tectonic settings of ophiolites in West Junggar, Xinjiang. *Geological Review* 38, 509–524 (in Chinese with English abstract).
- Zhang, H.F., Sun, M., Lu, F.X., Zhou, X.H., Zhou, M.F., Liu, Y.S., Zhang, G.H., 2001. Geochemical significance of a garnet lherzolite from the Dahongshan kimberlite, Yangtze Craton, southern China. *Geochemical Journal* 35, 315–331.
- Zhang, J.E., Xiao, W.J., Han, C.M., Ao, S.J., Yuan, C., Sun, M., Geng, H.Y., Zhao, G.C., Guo, Q.Q., Ma, C., 2011a. Kinematics and age constraints of deformation in a Late Carboniferous accretionary complex in Western Junggar, NW China. *Gondwana Research* 19, 958–974.
- Zhang, J.E., Xiao, W.J., Han, C.M., Mao, Q.G., Ao, S.J., Guo, Q.Q., Ma, C., 2011b. A Devonian to Carboniferous intra-oceanic subduction system in Western Junggar, NW China. *Lithos* 125, 592–606.

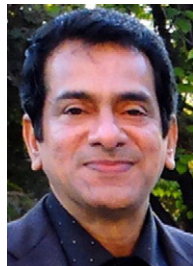
- Zhao, J.H., Zhou, M.F., 2007. Geochemistry of Neoproterozoic mafic intrusions in the Panzhihua district (Sichuan Province, SW China): implications for subduction-related metasomatism in the upper mantle. *Precambrian Research* 152, 27–47.
- Zheng, J.P., Sun, M., Zhao, G.C., Robinson, P.T., Wang, F.Z., 2007. Elemental and Sr–Nd–Pb isotopic geochemistry of Late Paleozoic volcanic rocks beneath the Junggar basin, NW China: implications for the formation and evolution of the basin basement. *Journal of Asian Earth Sciences* 29, 778–794.
- Zhou, T.F., Yuan, F., Fan, Y., Zhang, D.Y., Cooke, D., Zhao, G.C., 2008. Granites in the Saur region of the west Junggar, Xinjiang Province, China: geochronological and geochemical characteristics and their geodynamic significance. *Lithos* 106, 191–206.



Di Li is a PhD student of tectonics and basin structural geology at the School of Energy Resources, China University of Geosciences Beijing (CUGB). He received his BSc (2008) from Northwest University of China, and MSc (2011) from China University of Geosciences Beijing. He is mainly undertaking research using an integrated approach of geology, geophysics and geochemistry to reveal tectonic framework and filling evolution of the deep Junggar basin in the CAOB. He has published several papers in international and domestic journals.



Dengfa He is a Professor of basin structures and tectonics and petroleum geology at the School of Energy Resources, China University of Geosciences Beijing (CUGB). He received his BSc (1989) from Northwest University of China, MSc (1992) and PhD (1995) from PetroChina Research Institute of Petroleum Exploration and Development, Beijing. He finished his postdoc research at the Institute of Geophysics (now Institute of Geology and Geophysics), CAS, in 1997. His primary research interests focus on tectonics and basin evolution of the Central Asia and Tethyan tectonic domains. He has published 140 papers in international and domestic journals, and edited 12 memoir volumes and journal special issues. He is a recipient of the Science and Technology Award of the Ministry of Land and Resources (Second Prize, 2009) of China and the Beijing Science and Technology Award (Second Prize, 2004) of China.



M. Santosh is a Professor at the China University of Geosciences Beijing (China) and an Emeritus Professor at the Faculty of Science, Kochi University, Japan. He received his BSc (1978) from Kerala University, MSc (1981) from University of Roorkee, PhD (1986) from Cochin University of Science and Technology, DSc (1990) from Osaka City University and DSc (2012) from the University of Pretoria. He is the founding Editor of *Gondwana Research* as well as the founding Secretary General of the International Association for Gondwana Research. His research fields include petrology, fluid inclusions, geochemistry, geochronology and supercontinent tectonics. He had published over 450 research papers, edited several memoir volumes and journal special issues, and he is a co-author of the book 'Continents and Supercontinents' (Oxford University Press, 2004). He is a recipient of the National Mineral Award, Outstanding Geologist Award, Thomson Reuters 2012 Research Front Award, and Global Talent Award.



Delong Ma is a Master student of basin structural geology at the School of Energy Resources, China University of Geosciences Beijing (CUGB). He got his Bachelor's degree in China University of Geosciences Beijing, in 2011. His primary research interests are in Fault-Related Folding theory and structural explanation of foreland basins.